ELSEVIER

Overview of high-entropy oxide ceramics

Yitao Jiao [a], Jian Dai [b], Zhenhao Fan [b], Junye Cheng [c], Guangping Zheng [d], Lawan Grema [e], Junwen Zhong [f], Hai-Feng Li [a,*], Dawei Wang [b,*]

[a] Institute of Applied Physics and Materials Engineering, University of Macau, Macao SAR 999078, China
[b] School of Instrumentation Science and Engineering, Harbin Institute of Technology, Harbin 150080, China
[c] Department of Materials Science, Shenzhen MSU-BIT University, Shenzhen 517182, China
[d] Department of Mechanical Engineering, Hong Kong Polytechnic University, Hung Hom, Kowloon, Hong Kong, China
[e] Department of Mechanical Engineering, Ramat Polytechnic Maiduguri, Borno State, Nigeria
[f] Department of Electromechanical Engineering and Centre for Artificial Intelligence and Robotics, University of Macau, Macau SAR 999078, China

In 2004, Yeh and Cantor introduced high-entropy alloys (HEAs), which maximize configurational entropy by utilizing nearly equal elemental molar ratios. These HEAs are valuable for exploring the central regions of phase diagrams. Building on this concept, Rost et al. proposed entropy-stabilized oxides in 2015, revealing that high-entropy oxides (HEOs) exhibit structural stability driven by entropy. This article provides a comprehensive overview of HEOs, with a specific focus on high-entropy oxide ceramics (HEOCs). The paper explores the origins of the high-entropy concept and the fundamental effects of high-entropy materials. It examines entropy from its basic definition and investigates microscopic atomic distribution, crystal-level distortions, and electronic structures. Additionally, the article introduces theoretical prediction methods applied to high-entropy materials. Furthermore, this review systematically summarizes HEOCs, encompassing three key aspects: crystal structure, preparation methods, and performance applications. Finally, the review concludes by proposing future research directions based on the current progress in HEOCs.

Introduction

Entropy quantifies the level of disorder in a system. In 2004, Yeh and Cantor introduced the concept of entropy in alloys for exploratory research. High entropy alloys (HEAs) are characterized by their composition, which consists of more than five elements in approximately equal molar ratios [1]. The main objective in designing HEAs is to utilize entropy to promote the formation of a single phase. Based on the assumptions proposed by Boltzmann [2], a formula is developed to calculate the configurational entropy of solid solutions formed by equimolar elements. This development leads to qualitative and quantitative investigations into the concept of high entropy. Tsai and his colleagues consolidate their findings, highlighting four core effects [3] that distinguish HEAs from traditional alloys. These effects are:

(1) **High-entropy effect:** HEAs broaden the solubility limits between constituent elements, consequently promoting the formation of random solid solutions. This high-entropy effect amplifies the alloy's entropy value and enhances its thermal stability.
(2) **Slow diffusion effect:** In HEAs, the diffusion rates of elements are notably sluggish, which impedes the growth of secondary-phase nanoparticles. This reduces diffusion rate poses challenges in achieving refinement within the solid solution, resulting in a more uniform microstructure in the alloy.

* Corresponding authors.
E-mail addresses: Li, H.-F. (haifengli@um.edu.mo), Wang, D. (wangdawei102@gmail.com).

 https://doi.org/10.1016/j.mattod.2024.06.005

(3) **Severe lattice distortion:** Owing to variations in atomic radii and electronegativity among the elements in HEAs, pronounced lattice distortion occurs. This distortion contributes to the material's reinforcement and hardening, thereby improving its mechanical properties.

(4) **Cocktail effect:** HEAs employ a blend of diverse elements to create a complex alloy system. This cocktail effect imparts unexpected and superior properties to the alloys, surpassing those of single-element alloys. These distinctive combinations of properties give rise to the development of novel materials, showcasing excellent specific strength, enduring high strength at elevated temperatures, possessing high and low-temperature fracture toughness, rational wear, and corrosion resistance, augmented magnetic thermal effects, superconductivity, etc.

The concept of entropy quickly extends to other material systems. Ceramics, in comparison to metals, have a wide range of microstructures, which provides a strong basis for innovation in the structure and performance of high-entropy ceramics (HECs). Initially, early studies on high-entropy ceramic materials focused mainly on thin-film materials composed of nitrides. These nitride films with high entropy are produced through magnetron sputtering on high-entropy alloy targets in an argon and nitrogen atmosphere [4]. The first single-phase film of this kind is known as (AlCrTaTiZr)N [5].

In 2015, Christina M. Rost and her team examined and summarized the concept of entropy-stabilized oxides [6]. As research progresses, high-entropy characteristics play a crucial role in the field of ceramics. Similar to HEAs, HEOCs are formally defined as solid solutions consisting of more than five cation or anion sublattices, demonstrating high configurational entropy [6].

HEOCs reside in the central area of the phase diagram and possess the possibility of revealing unexpected properties. These HEOCs attract significant attention, leading to diverse research avenues exploring aspects such as microstructure, compositional design, and crystal structure, among others. The remarkable performance potential of HEOCs generate considerable interest across various application fields, including lithium-ion batteries, supercapacitors, water splitting, catalysis, and more. In these scenarios, HEOs and HEOCs (as depicted in Fig. 1) have exhibited superior performance when compared to traditional materials [7].

In recent years, the number of publications on HEOCs has increased significantly (Fig. 2), marking the rapid growth of this emerging field. This paper provides a comprehensive review of HEOCs. It commences with an exploration of the entropy concept, delving into the theoretical underpinnings of entropy sta-

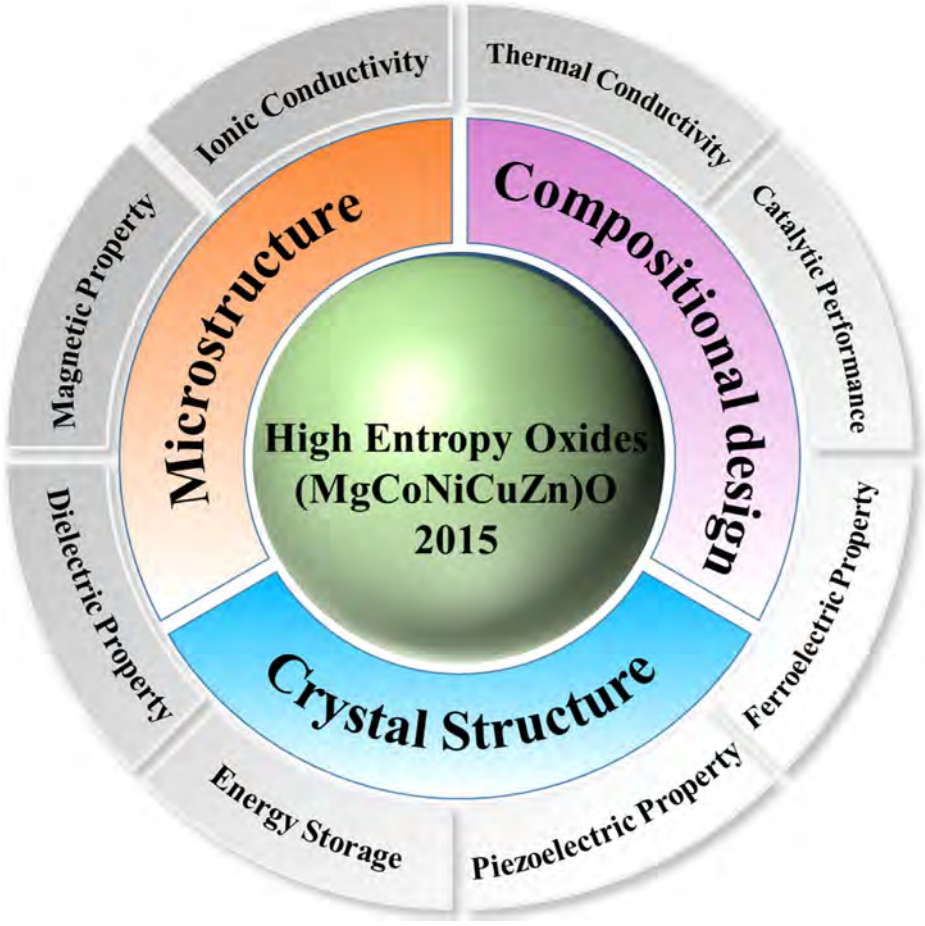

FIG. 1

The development of HEOs and HEOCs.

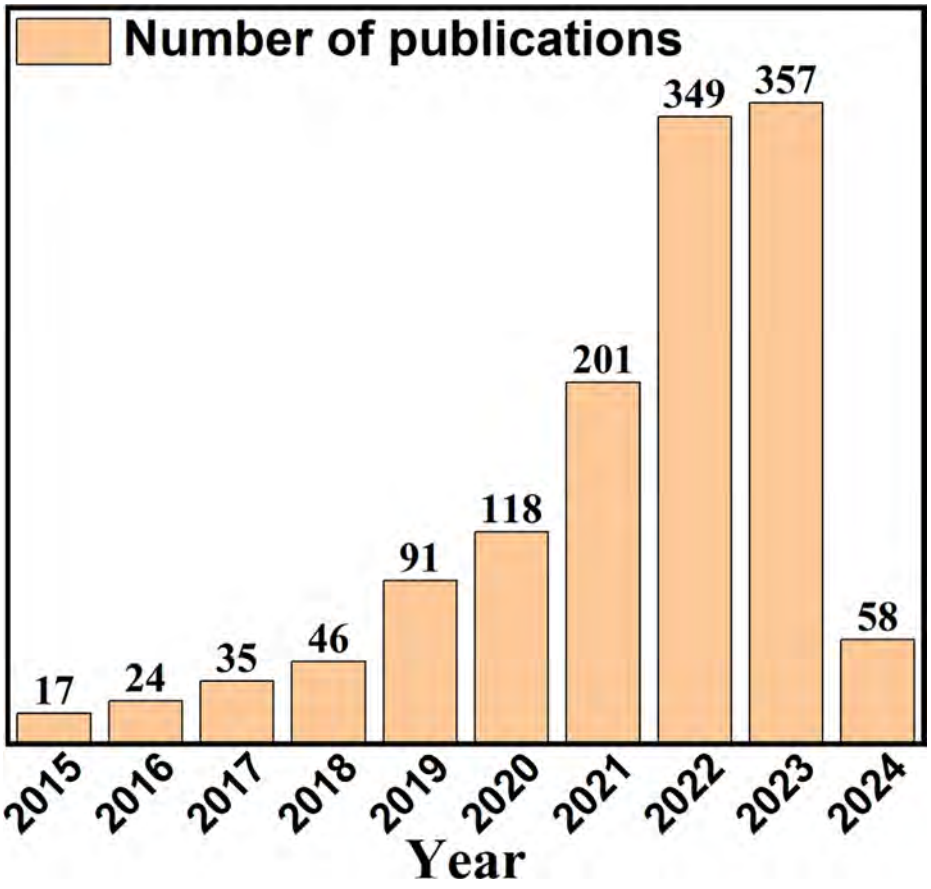

FIG. 2

Number of publications per year about HEOCs (Data from Web of Science on April 1, 2024 using keywords: "high entropy" and "oxide ceramics" or "high entropy" and "oxide" and "ceramics").

bility. Additionally, it outlines the primary methods used for predicting structures and properties of HEOCs. A summary of the key crystal structures, preparation techniques, and properties of HEOCs is carried out. The role of entropy effects in various properties can be better understood by examining specific examples. Lastly, potential avenues for future research are explored and discussed.

High entropy principle

Definition of entropy

The concept of entropy was first proposed by German physicist Rudolf Clausius in 1850. Clausius defines entropy as the degree of disorder of a thermodynamic system, which is used to describe the degree of disorder of the system [1]. For high entropy systems, the calculation of entropy is essential. The mixing entropy of HEOs can be calculated in the ideal situation using the following equation [2]:

$$\Delta S_{mix} = -R\Sigma x_i ln(x_i) \quad (1)$$

where ΔS_{mix} is the mixing entropy, R is the gas constant, and x_i is the mole fraction of the i-th component in the HEOs.

In the ideal situation, it is assumed that the HEOs are perfectly mixed and that there are no interactions between the different components. This means that the energy of the HEOs is simply the sum of the energies of the individual components, and the mixing entropy can be calculated based on the statistical probability of the different arrangements of the constituent atoms. When calculating the mixing entropy of equiatomic HEOs – where each constituent element has an equal atomic fraction – the equation for calculating the mixing entropy can be simplified.

Simplifying the above equation, the formula for calculating the entropy of mix with equimolar ratio is [8]:

$$\Delta S_{mix} = RlnN \quad (2)$$

Where N is the number of elements, and R is the gas constant: 8.314 J/K·mol [1].

This simplified equation for mixing entropy of equiatomic HEOs shows that the mixing entropy is directly proportional to the natural logarithm of N. This means that the mixing entropy increases with increasing N, which can promote the formation of a single-phase solid solution in equiatomic HEOs. Through the above formula, the mixing entropy of the material system can be simply calculated [8]. For example, when the N of element types is equal to 4, 5, 6, and 7, the corresponding ΔS_{mix} is equal to 1.39R, 1.61R, 1.79R, and 1.96R (Fig. 3a).

In a system consisting of multiple elements and atoms, HEAs exhibit a distinct characteristic compared to HEOs. In HEAs, the elements are randomly distributed, whereas in HEOs, the oxygen atoms within the sublattice do not contribute to the system's entropy in an ideal state, resulting in an ordered distribution.

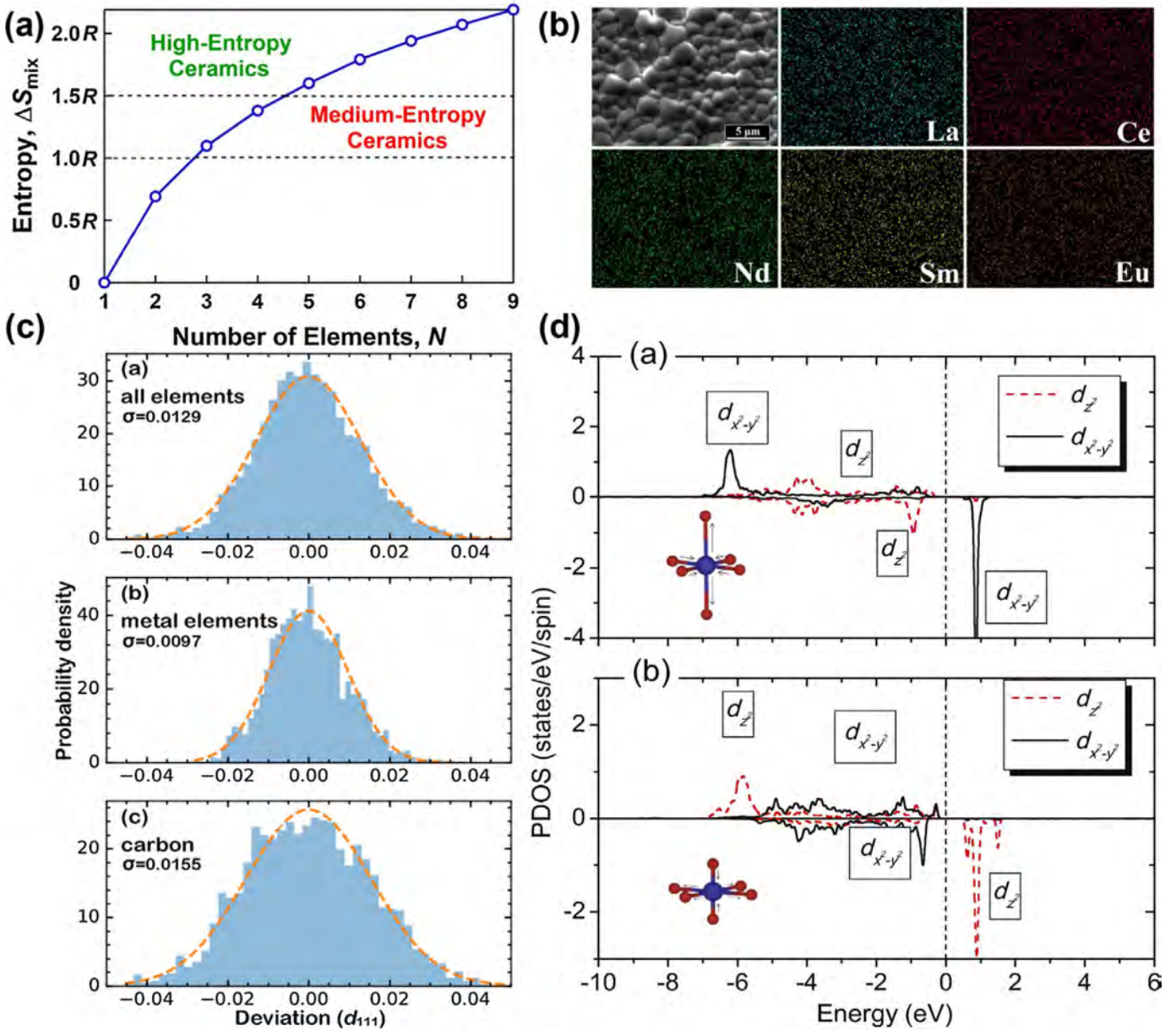

FIG. 3

(a) The relationship between entropy value and the number of elements and the distribution area of medium and high entropy ceramics[8]; (b) SEM image and EDS elemental mappings of $(La_{0.2}Ce_{0.2}Nd_{0.2}Sm_{0.2}Eu_{0.2})_2Zr_2O_7$[10]; (c) Statistical information on atom deviations illustrates significant deviation of carbon from its ideal position[20]; (d) Different electronic ground states correspond to different copper-oxygen octahedra [22].

For example, HEO, in which the five metallic elements A, B, C, D, and E, combine with oxygen to form 1 mol of $(A_{0.2}B_{0.2}C_{0.2}D_{0.2}E_{0.2})O$. The entropy value of this HEO, calculated using the traditional formula, would be approximately 1.61*R*. Similarly, when ABCDE forms 1 mol of a high-entropy alloy, the entropy value also equals 1.61*R* [9]. This reveals an interesting phenomenon: the presence of oxygen reduces the amount of each metal element required to achieve an entropy value of 1.61*R* from 1 mol to just 0.2 mol. Thus, the total number of atoms does have an impact on entropy value. The conventional mixed entropy formula, therefore, becomes a subject of controversy when estimating the entropy value of HEOs [9].

Microscopic atomic distribution

In HEOCs, the arrangement of cations displays a more consistent distribution at the atomic level due to the presence of ordered sublattices. Each cation lattice site in these ceramics shares a similar environment, known as quasi-equivalent sites, which play a crucial role in achieving the uniform distribution of cations. This even distribution, resulting from the entropy effect, contributes to the stability of the crystal structure. The atomic-level homogeneity is verified through observations using scanning electron microscopy (SEM) with energy dispersive X-ray spectroscopy (EDS) system [10–12] (as shown in Fig. 3b). Additionally, advanced techniques such as scanning electron transmission

microscopy (STEM) and atom probe tomography (APT) are utilized to analyze the elemental distribution in HEOCs, demonstrating the absence of significant aggregation [13–18].

Crystal microscopic distortion

Within a high-entropy system, the varying sizes and electronegativity of different atoms lead to lattice distortion. Rost et al. [6,19] utilized fitted extended X-ray absorption fine structure (EXAFS) data to investigate atomic distances in the $(Mg_{0.2}Ni_{0.2}Co_{0.2}Cu_{0.2}Zn_{0.2})O$ system. Their findings reveal that the distances between cations are consistent, whereas the distances between each cation and oxygen ion are not uniform. Density functional theory (DFT) calculations demonstrate that the anions (oxygen elements) deviate from their ideal sublattice positions to accommodate lattice distortion, while the assortment of cations is uniformly distributed on the face-centered cubic (FCC) sublattice [20]. A similar phenomenon is observed in the structure prediction of the carbide HEC $(Zr_{0.2}Hf_{0.2}Ti_{0.2}Nb_{0.2}Ta_{0.2})C$, where the displacement of carbon atoms is more pronounced compared to metal ions (refer to Fig. 3c) [20].

Electronic structure engineering

The macroscopic properties displayed by materials are closely related to their microscopic electron layer structure. The mixture of various metal elements in HEOCs create a large degree of flexibility in their electronic structure. Advances in theoretical calculations enable the prediction of the electronic structure between different elements in materials, facilitating the explanation and analysis of their macroscopic properties. The electronic structures of HEOCs are being predicted through the application of DFT. Calculating electronic structures using DFT requires an input crystal structure, which can be challenging for high-entropy ceramic oxides due to their complex and disordered nature. To eliminate periodic errors in completely disordered structures, a unit cell large enough to contain lattice distortions must be used [21]. To simulate the random structure of HEOs, Rak et al. [22] used a rock-salt supercell containing 480 atoms and performed Bader charge and density of states analyses. In (MgCoCuNiZn)O, the addition of Sc causes Cu to shift significantly from their ideal lattice positions, while the addition of Li oxidizes CoNiCu but did not significantly change their lattice positions [23]. Under the same model, the density of states of $(Mg_{0.2}Co_{0.2}Cu_{0.2}Ni_{0.2}Zn_{0.2})O$ is calculated, which finds that the octahedron (CuO_6) composed of copper and oxygen has a certain degree of deformation (Fig. 3d). Different electronic ground states of copper ions correspond to different copper-oxygen octahedral shapes. When electrons fill half of the d_{xy}^2 orbitals, the octahedron is elongated; when electrons fill half of the d_z^2 orbitals, the octahedron is Jahn-Teller compressed [22].

Supercells serve as a valuable tool for examining high-entropy systems; however, performing large-scale calculations can be challenging due to their demanding nature in terms of supercomputing power. To mitigate this challenge, the special quasi-random structure (SQS) is introduced to theoretically describe the structure of HEOCs [24,25]. The essence of the SQS approach lies in constructing a specialized periodic structure that reduces the number of atoms in a single unit cell, thus enhancing computational feasibility. In a study by Liu et al. [26], SQS supercells are utilized to investigate $Zn_{0.1}Ca_{0.1}Sr_{0.4}Ba_{0.4}ZrO_3$. By reducing the number of atoms per unit cell to 100, they succeed in significantly alleviating computational complexity. Their research illustrates that high-entropy effects within HEOs can lead to non-uniform chemical bonding and lattice distortion. Despite the cost reduction achieves through SQS quasi-random structures, caution must be exercised in their application. The SQS approach considers interactions between ions that are widely separated to have negligible influence on the system, potentially resulting in significant errors, particularly for important long-range interactions [27].

Theoretical prediction

The synthesizable properties and stability of HEAs can be predicted through theoretical calculations. Several methods, including DFT, molecular dynamics (MD), and CALPHAD, are successfully applied to this field. DFT can use various descriptor. As to predict single phases in HECs. When combined with the SQS supercell technique (Fig. 4a,b), calculation difficulty and scale can be reduced while maintaining rationality[28,29].

Pitike et al. [30] proposed a general evaluation method that has been validated for 56 multicomponent single-phase compounds. This method uses the nearest neighbor model (NNM), and the corresponding parameters can be obtained from two-component oxides, thereby reducing the need for DFT calculations. To evaluate the utility of the approach, they compare the predicted combinations with the experimentally observed entropy-stabilized oxide (MgCoCuNiZn)O. The strength of molecular dynamics (MD) lies in the simultaneous treatment of thousands of atoms. The accuracy of this method is determined by the interatomic potential energy. Anand et al. [31] explored the role of configurational entropy in single-phase multicomponent oxides. They calculate the enthalpies and free energies of these oxides to determine their stability, and investigate changes in enthalpy, entropy (Fig. 4d), and ion distance as the number of cations increased, quantifying lattice distortion (Fig. 4c).

In addition to the theoretical calculation methods mentioned earlier, machine learning emerges as a promising tool in the study of HEOCs. Machine learning techniques, including artificial neural networks and support vector regression, are being applied to predict material properties, design novel HEOCs, and optimize processing parameters. Kaufmann et al. [32] harnessed machine-learning techniques to forecast the behavior of high-entropy carbide ceramics. They utilize thermodynamic parameters and material composition to anticipate the entropy stability of high-entropy carbide ceramics. Some of the forecasted components are validated through density functional theory calculations and experimental synthesis. This research also sheds light on the potential of machine learning in the prediction of HEOCs.

Crystal structure

Most elements in HEAs adopt either a BCC or FCC structure, resulting in HEAs with predominantly BCC or FCC structures [33]. Unlike traditional ceramics composed of a single primary element, HEOCs incorporate multiple elements in equimolar or near-equimolar ratios, leading to the formation of complex crys-

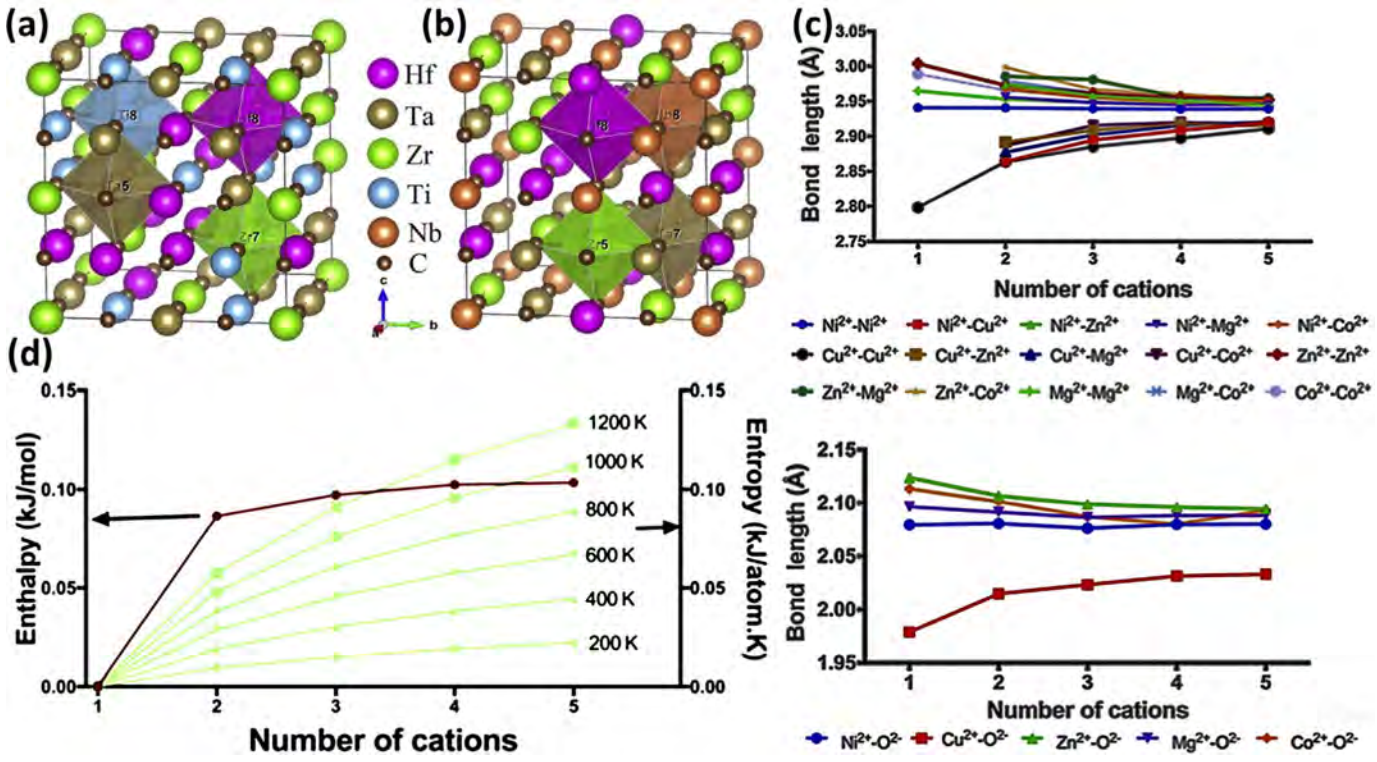

FIG. 4

The optimized crystal structures of 2 × 2 × 2 SQS supercell for (a) (HfTaZrTi)C and (b) (HfTaZrNb)C [29]; (c) Variation in enthalpy and configurational entropy with number of cations [31]; (d) Variation in bond length with an increase in the number of cations for cation-cation pairs and cation–anion pairs [31].

tal structures. HEOCs possess a rich variety of crystalline structures, including rock-salt [34–40], fluorite [41–48], perovskite [49–54], spinel [55–59], pyrochlore [60–63], and olivine [64,65] structures. The intricate nature of high-entropy systems, characterized by a diverse range of cation combinations, introduces a multitude of variables that impact the prediction and identification of crystal structures. The presence of multiple cations with varying ionic radii introduces disorder and complexity into the crystal lattice, resulting in the formation of solid solutions, intermetallic compounds, or even amorphous phases. This complexity underscores the heightened research interest surrounding high-entropy systems within the academic community.

Rock-salt

Rock salt is a basic crystal structure commonly found in various oxides. HEOCs with a rock-salt structure demonstrate notable characteristics such as high ionic conductivity [36] and a high dielectric constant [66]. Several HEOCs and their variations with a rock-salt structure (as depicted in Fig. 5a) are derived from (MgCoNiCuZn)O [8], which is the initial entropy-stabilized oxide reported. This discovery highlights the promising potential of configurational entropy in producing single-phase oxides [6].

Rost et al. compared the X-ray diffraction (XRD) data for five-element and four-element oxides (Fig. 5b) and found that the oxide tended to be single-phase as the number of elements increased.

In a subsequent investigation, Rost et al. [19] utilized the EXAFS technique to examine the rock-salt structure of HEOCs. The findings reveal that the local bond lengths between each cation and the oxygen ion varies, while the distances between cations are relatively consistent. The cations exhibit a uniform distribution on the face-centered cubic (FCC) sublattice, with the distortion of the Cu–O polyhedron being more pronounced. The experimental results are supported by DFT calculations, which indicates that the oxygen ions shifted from their ideal positions to accommodate the distortion of the cation polyhedron.

Berardan et al. [67] thoroughly explored the crystal structure of HEOCs based on (MgCoNiCuZn)O, examining the impact of synthesis conditions, stoichiometry, and post-annealing treatments. Through electron paramagnetic resonance (EPR) and XRD studies, they uncover the unique role of copper in distorting and disordering the randomly distributed rock-salt structures. The local environment of copper shifts from octahedral to rhombohedral, depending on the thermal history of the samples, leading to deviations from the ideal rock-salt structure. The extent of distortion and disorder in the crystal structure, which can be fine-tuned through post-annealing treatments, greatly influences the dielectric properties of the material. These findings provide valuable insights into the behavior of this innovative material category and offer new possibilities for manipulating the functional properties of compounds based on (MgCoNiCuZn)O by controlling the evolution of their crystal structure.

Fluorite

Ever since entropy-stabilized rock-salt oxides were introduced [6], researchers expand their exploration of entropy to include other oxide structures. Fluorite-structured rare earth oxides are

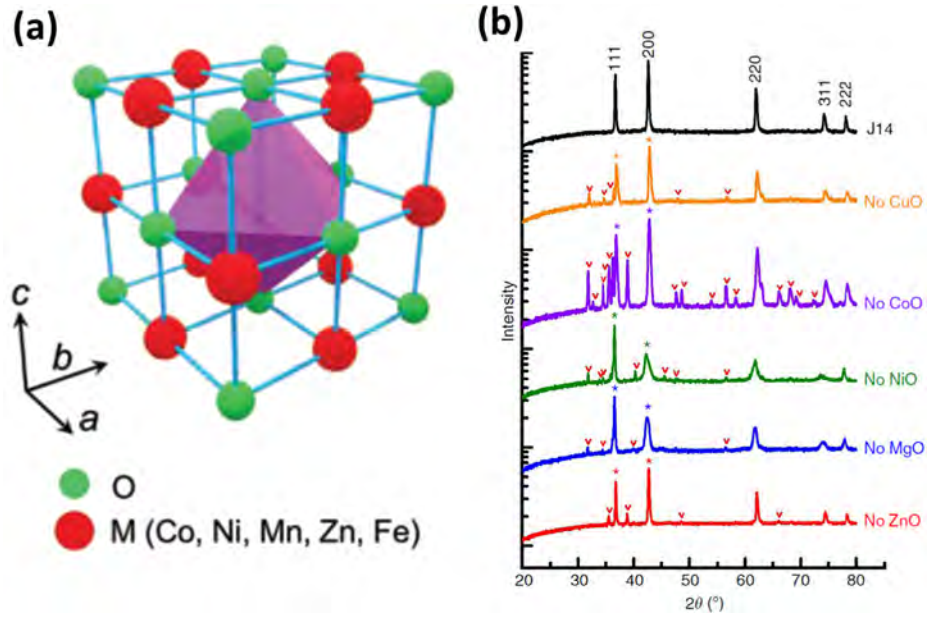

FIG. 5

(a) Rock-salt (Cubic) with space group Fm-3 m [34]; (b) XRD chart of five element oxides and four element oxides (J14 is (MgCoNiCuZn)O) [6].

widely recognized for their strong functional properties, and the concept of entropy has opened new avenues for their synthesis and preparation.

When it comes to synthesizing high-entropy fluorite oxides, several fundamental principles need to be followed. Firstly, the constituent cations that make up these high-entropy fluorite oxides (as depicted in Fig. 6a) should have similar radii, aligning with the characteristics of high-entropy rock-salt oxides. Secondly, the reactants employed should encompass two or more distinct oxide crystal types. Lastly, it is crucial that at least one oxide remains immiscible with other cationic oxides [8].

Sarkar et al. [43] made the discovery that Ce^{4+} plays a vital role in stabilizing high-entropy fluorite oxides. Building on this concept, more high-entropy fluorite oxides have been synthesized [41,4269,70]. These high-entropy fluorite oxides can be categorized into three primary molecular formulas: $(CeRE)O_{2-\delta}$ [7], $(HfZrCeM)O_{2-\delta}$ [7], and $RE_2TM_2O_7$ [71]. In these formulas, RE represents Rare Earth Element, TM represents transition metal, M represents other metal elements, and δ depends on the valence of the cation. The molecular structure of $RE_2TM_2O_7$ relies on the ratio of the ion radius of rare earth elements to the ion radius of transition metals. A general formula exhibiting a pyrochlore

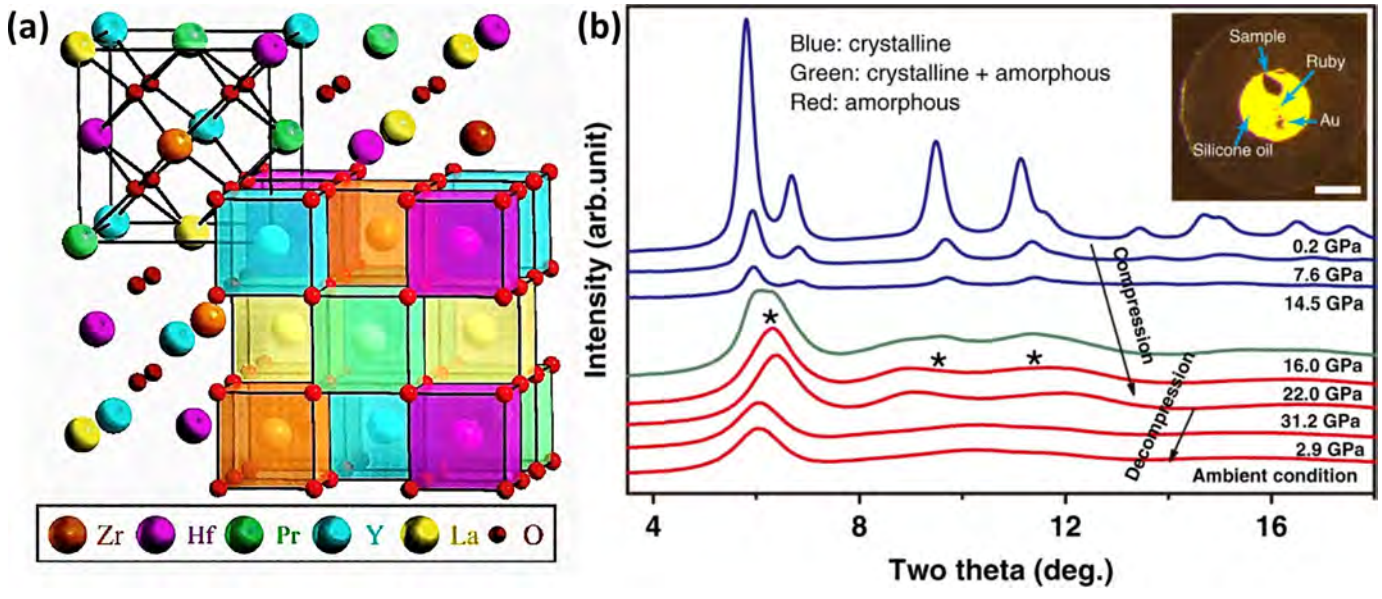

FIG. 6

(a) Fluorite (Cubic) with space group Fm-3 m [48]; (b) Representative XRD patterns of (Ce,La,Pr,Sm,Y)O during compression and decompression at room temperature [68].

structure is formed when the ratio falls within the range of 1.46 to 1.78. Conversely, when the ratio is exactly 1.46, the general formula adopts a fluorite structure [71].

Cheng et al. [68] employed the nebulizing spray pyrolysis (NSP) method to synthesize $(Ce_{0.2}La_{0.2}Pr_{0.2}Sm_{0.2}Y_{0.2})O_{2-\delta}$ powders and characterized them through the use of a chromatic-aberration-corrected High-Resolution Transmission Electron Microscope (HRTEM) and synchrotron high-energy XRD (Fig. 6b). The findings confirm that the sample possesses a fluorite structure. The most significant observation in this study is that pressure application allows for the control of crystal lattice distortion, resulting in changes in bond angles and continuous modifications in the band gap. Excessive alterations in bond angles can disrupt the long-range order of the lattice, leading to amorphization. When the pressure is reduced, a portion of the amorphous phase reverts to the crystalline state, forming a hybrid HEOC composed of glass-nanoceramics. This investigation enhances our comprehension and application of the structure and properties of HEOCs.

Sang et al. [72] investigated the structure and properties of equimolar quaternary HEOC $(Gd_{0.25}Sm_{0.25}Yb_{0.25}Y_{0.25})_3TaO_7$. They use a preparation process that combined sol–gel technology and high-temperature calcination to successfully prepare high-entropy fluorite oxide nano-powders and dense bulk samples. The thermal properties of the sample are analyzed, and it is found that the sample had low thermal conductivity (1.170–1.211 $W{\cdot}m^{-1}{\cdot}K^{-1}$, from 50 to 1000 °C). This is due to the coexistence of multiple ions that promote anharmonic vibration and lattice distortion effects of phonons. The sample still exhibit excellent phase stability at 1400 °C, indicating that high-entropy fluorite oxide is a promising material for thermal barrier coatings.

Xu et al. [41] proposed a new radiation-resistant high-entropy fluorite oxide, $(Nd_{0.2}Sm_{0.2}Gd_{0.2}Dy_{0.2}Er_{0.2})_2Ce_2O_7$. The sample is synthesized using the traditional solid-state method, and the reactant mixed powder is subjected to two pressing processes with different pressures. After 9-MeV Au ion irradiation with an ion fluence of 2.7×10^{15} and 4.5×10^{15} ions/cm^2, no phase transition or decomposition occurs in the sample. The degree of amorphization and lattice expansion of the material is much lower than that of $Nd_2Ce_2O_7$, which indicates that the material has strong radiation-resistant properties.

Perovskite

Molecules of the perovskite configuration have become a hot topic of research in recent years due to their chemical and structural properties [73]. The perovskite structure is undoubtedly an important part of the extension of the entropy concept to HEOC systems (Fig. 7 a-e). The classical chalcogenide structure consists of two cations involved [74], with the structural general formula ABO_3. the stability of the perovskite structure is assessed by the Goldschmid tolerance factor (t) [75]. The formula is as follows:

$$t = \frac{R_A + R_O}{\sqrt{2}(R_B + R_O)} \tag{3}$$

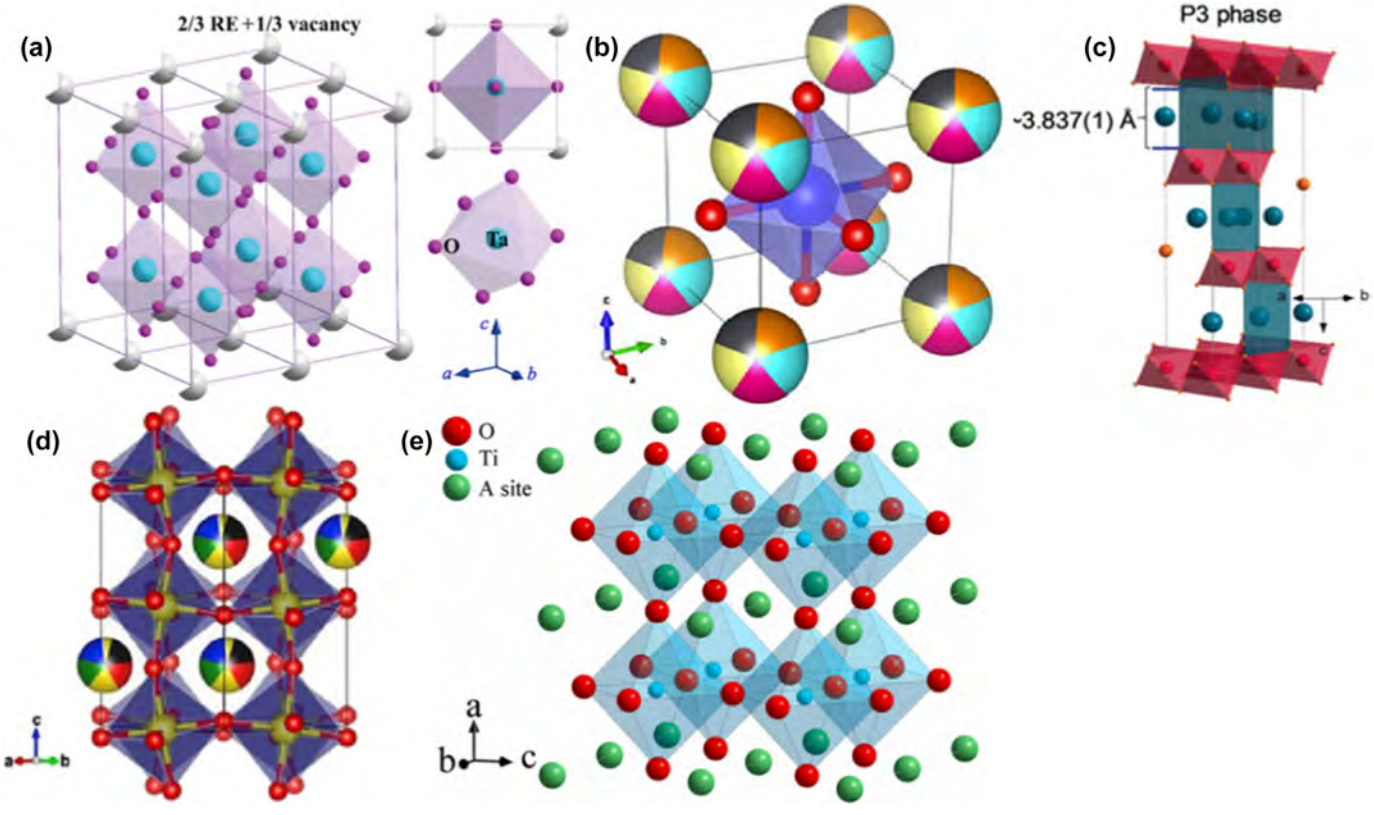

FIG. 7

(a) Perovskite (Tetragonal) with space group P4/mmm [49]; (b) Perovskite (Cubic) with space group Pm-3 m [50]; (c) Perovskite (Hexagonal) with space group R3m [53]; (d) Perovskite (Orthorhombic) with space group Pbnm [54]; (e) Perovskite (Tetragonal) with space group P4mm [51].

where R_A, R_B and R_O refer to the radius of the A cations, B cations and oxygen anion, respectively. When the value of t is greater than 0.75 and less than 1, the perovskite structure is stable. When the value of t approximates 1, the perovskite shows a cubic phase [76].

Efforts have aimed to explore numerous properties of high-entropy oxide ceramics with perovskite structure, offering novel insights for a range of fields. Key properties investigated include ferroelectric properties [51], optical properties [77], magnetic properties [78], energy storage properties [79], magneto-thermal properties [80], dielectric properties [81], photocatalytic hydrogen evolution [82], and thermoelectric properties [83].

Furthermore, the overall performance of the material can be enhanced by utilizing high-entropy perovskite oxides as a monolithic unit for doping known matrix materials. Zhou et al. [84] first doped $Bi(Zn_{0.2}Mg_{0.2}Al_{0.2}Sn_{0.2}Zr_{0.2})O_3$ (BZMASZ) into $BaTiO_3$-$Na_{0.5}Bi_{0.5}TiO_3$ (BT-NBT). This introduction of BZMASZ leads to a transformation of the material from a tetragonal phase to a cubic phase. Simultaneously, the incorporation of HEOCs enhances the relaxation behavior and formation of local nanodomains. Excellent temperature stability is observed in ceramics with a composition of 0.9(0.75BT-0.25NBT)-0.1BZMASZ.

Spinel

Spinel, a significant oxide structure, can be described by the general formula AB_2O_4. It demonstrates a cubic closed-packed (CCP) configuration of oxygen atoms, with the A-site cations occupying tetrahedral positions and the B-site cations residing in octahedral positions [111]. The remarkable feature of spinel is its high entropy, as illustrated in Fig. 8, which enables it to accommodate multiple cations simultaneously within a single unit cell. However, it is worth mentioning that achieving single-phase spinel poses a substantial challenge [8].

Dąbrowa et al [85] synthesized the first high-entropy single-phase spinel oxide – $(Co, Cr, Fe, Mn, Ni)_3O_4$. Stygar et al [86] have investigated different combinations of components in the Co-Cr-Fe-Mg-Mn-Ni-O system. Three combinations of single-phase spinel structures are identified, namely Co-Cr-Fe-Mn-Ni-O, Cr-Fe-Mg-Mn-Ni-O, and Co-Cr-Fe-Mg-Mn-O. Two high-entropy spinel components, $(Cr,Fe,Mg,Mn,Ni)_3O_4$ and $(Co,Cr,Fe,Mg,Mn)_3O_4$, are discovered for the first time. It is observed that the synthesis temperature for high-entropy spinel must be carefully chosen. This is because the content of the rock salt phase significantly increases in Co-Cr-Fe-Mg-Mn-Ni-O, Co-Fe-Mg-Mn-Ni-O, Co-Cr-Fe-Mg-Ni-O, and Co-Cr-Mg-Mn-Ni at sintering temperatures of 900 °C and 1100 °C. As the rules for synthesizing high-entropy spinel become more established, various synthetic methods are developed and improved [86].

Bian et al. [87] successfully synthesized the high-entropy spinel oxide $[(FeCoNiMn)_{1-x}Na_x]_3O_4$ using the SP technique. Analysis of the XRD patterns confirms the presence of a spinel structure, exhibiting a space group of Fd-3 m. As the Na ion con-

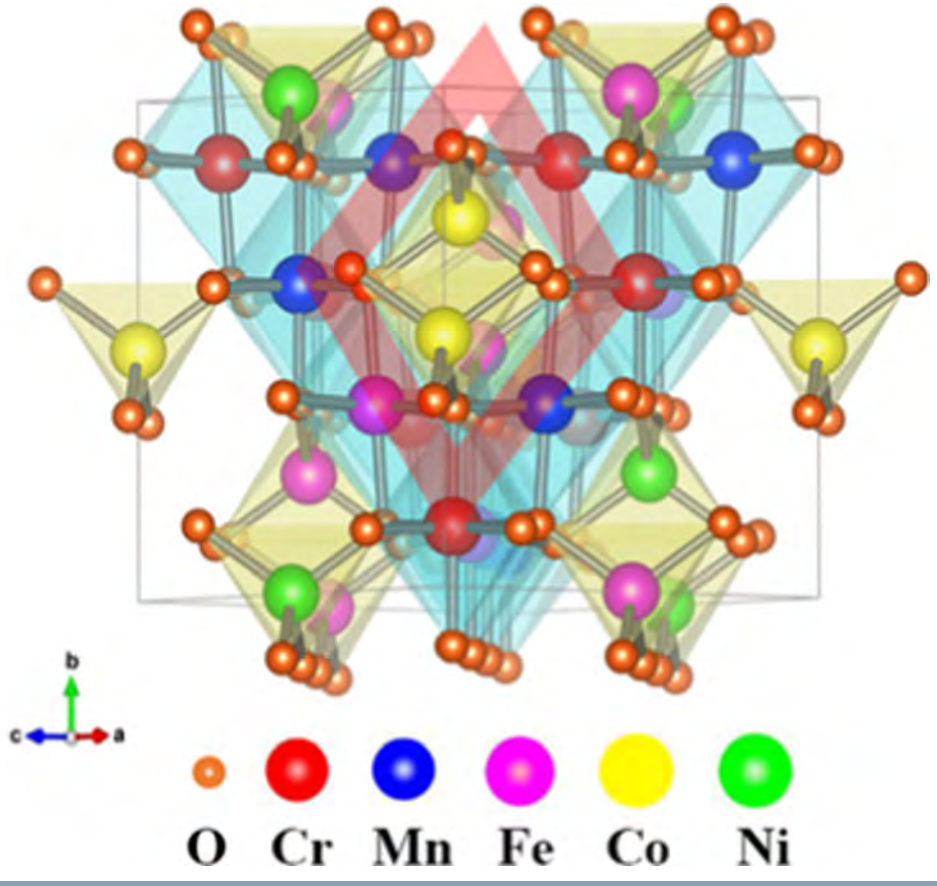

FIG. 8

Spinel (Cubic) with space group Fd-3 m [55].

tent increases, a reduction in the lattice constant is observed. High-resolution transmission electron microscopy (HRTEM) reveals lattice spacings of 0.209 nm, 0.342 nm, 0.628 nm, and 0.484 nm, corresponding to the crystal planes (111), (220), (511), and (400), respectively, which is consistent with the findings obtained from XRD analysis.

Pyrochlore

Pyrochlore is a structure related to the fluorite configuration. Informally, pyrochlore is more like an anion-deficient (ideally, it is one-eighth tetrahedral anion-site vacant) distorted fluorite [88]. The high entropy of pyrochlore has also become a new research direction for researchers.

Jiang et al. [60] reported for the first time the HEO $Nd_2(Ti_{0.2}Nb_{0.2}Sn_{0.2}Hf_{0.2}Zr_{0.2})_2O_{7+x}$ and $Nd_2(Ta_{0.2}Sc_{0.2}Sn_{0.2}Hf_{0.2}Zr_{0.2})_2O_7$ with pyrochlore structure (Fig. 9). They analyze the local structure of the high entropy pyrochlore structure by neutron diffraction (ND) and pair distribution functions (PDF). The results show that the average structure of high entropy pyrochlore is orthorhombic Imma. The local TiO_6 octahedron in $Nd_2(Ti_{0.2}Nb_{0.2}Sn_{0.2}Hf_{0.2}Zr_{0.2})_2O_{7+x}$ appears to be noticeably distorted, and there is some degree of titanium clustering. Conversely, when observing the microstructure of $Nd_2(Ta_{0.2}Sc_{0.2}Sn_{0.2}Hf_{0.2}Zr_{0.2})_2O_7$, it is discovered that the cations are uniformly and randomly distributed. These two pure-phase high-entropy pyrochlore structures have contrasting morphological characteristics on a microscopic scale. This indicates that cations in HEOCs may not adhere to the rule of average random distribution.

Mao et al. [89] reported on an ultrafast oxide densification method that successfully prepared high entropy pyrochlore oxide $(La_{0.2}Nd_{0.2}Sm_{0.2}Eu_{0.2}Gd_{0.2})_2Zr_2O_7$. The preparation of pyrochlore-type HEOCs typically requires high temperatures for several hours to achieve the desired density. In this study, the researchers utilize the reactive flash sintering (RFS) method to prepare high entropy pyrochlore oxides in just seconds at 1200 °C. XRD data shows that the product structure corresponds to the peak structure of pyrochlore. The lattice constants are also consistent with products prepared by traditional sintering process. The density of the product reaches 99 % of that obtained

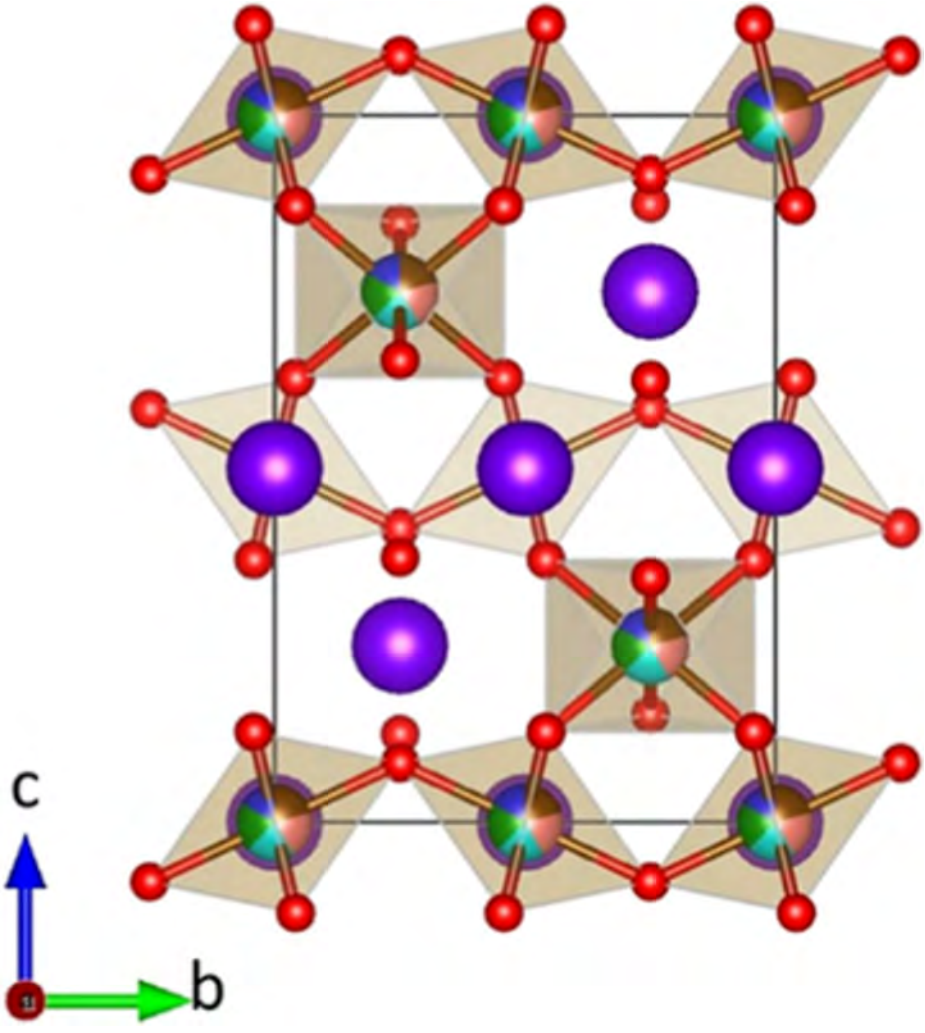

FIG. 9

Pyrochlore (orthorhombic) with space group Imma [60].

by the traditional solid-state method (1600 °C, 6h). Characterization by SEM-EDS confirm the homogeneous composition of pyrochlore-type HEOs at the atomic level.

Other oxide structure

More HEO structures (Fig. 10) are unearthed. Vinnik et al. [90] sintered the oxide and carbonate at 1400 °C to obtain a high-entropy single-phase oxide with a magnetoplumbite structure – $Ba(Fe_6Ti_{1.2}Co_{1.2}In_{1.2}Ga_{1.2}Cr_{1.2})O_{19}$. Tseng et al. [91] successfully prepared HEOCs of bixbyite structure –$Gd_{0.4}Tb_{0.4}Dy_{0.4}$-$Ho_{0.4}Er_{0.4}O_3$ using the polymeric steric entrapment method. The HEOC exhibits a stable single-phase structure from room temperature to 1650 °C. Zhao et al. [92] prepared a promising high temperature insulation material-$(Ti,Zr,Hf)P_2O_7$. The sample is a cubic metal pyrophosphate structure with good thermal stability and low thermal conductivity (0.78 $W{\cdot}m^{-1}{\cdot}K^{-1}$).

Preparation methods

From the inception of the concept of entropy stabilization to the successful synthesis of HEOCs, the method of preparation plays a pivotal role. Different synthesis methods yield varying impacts on the final product, influencing factors such as microstructure, performance parameters, structural stability, and more. Even within the same synthesis method, the manipulation of parameters allows for further optimization of product morphology and performance [8]. For instance, while solid-state synthesis methods offer simplicity and scalability, they may result in heterogeneous mixing and phase segregation due to the high melting points of some oxide precursors. Conversely, sol–gel processing provides better control over homogeneity and nanostructure formation but requires careful manipulation of precursor chemistry and drying conditions to prevent phase separation and densification issues [138,149]. Moreover, reaction time, as the most intuitive parameter, exerts a significant influence on the microstructure of high-entropy products [103,108]. It is established that systems exhibiting varying entropy levels necessitate distinct optimal reaction parameters. Longer reaction times often facilitate the attainment of equilibrium phases and finer microstructures through enhanced diffusion and homogenization processes, while shorter reaction times may result in incomplete reactions and phase transformations [105,106]. The integration of diverse preparation techniques has catalyzed a novel research domain focusing on determining the ideal reaction conditions for high-entropy systems. Researchers are increasingly exploring innovative approaches such as Co-precipitation (CP) [119], Solution combustion (SC) [146] and Spark plasma sintering (SPS) [110] to tailor the microstructure and properties of HEOCs for specific applications. By elucidating the underlying mechanisms governing the preparation methods and their effects on the structure–property relationships of HEOCs, researchers can accelerate the development of next-generation ceramic materials with tailored functionalities for diverse technological applications.

The methods for preparing HEOs can be categorized into three main groups: solid-state methods (such as SSR, OFZG, RFS, and SPS), liquid-phase methods (including CP, RCP, solvothermal synthesis, SC, SGSC, and SP), and gas-phase methods (such as RS and PLD) [8]. The summary of these preparation methods can be found in Table 1.

Solid-state reaction (SSR)

Among the customary manufactured methodologies, SSR (Fig. 11a) is extensively utilized in the fabrication of diverse HEOCs [61,86,93–98]. The fundamental procedure of SSR can be partitioned into two segments: blending and dissemination. Among these, blending can be accomplished using the ball milling technique. Ball milling involves the mixing and grinding of powders with an optimal ratio and distinct balls within a receptacle based on a specified mass ratio. As the receptacle rotates on the roller, the balls impel the precursor powder to continuously roll inside the receptacle, thereby facilitating the process of blending. The mixed powder then undergoes a sintering

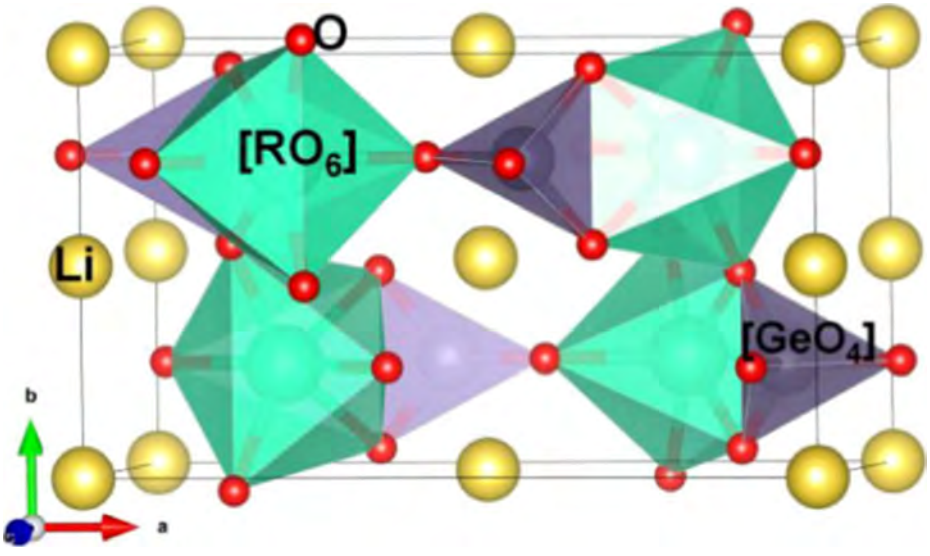

FIG. 10

Olivine (orthorhombic) with space group Pnma [64].

TABLE 1

Various synthetic methods and corresponding products.

Preparation	Composition	Feature	Ref.
Solid-state reaction	$(La_{0.2}Nd_{0.2}Sm_{0.2}Eu_{0.2}Gd_{0.2})_2Zr_2O_7$	low thermal conductivity	[61]
	$(Co,Cr,Fe,Mn,Ni)_3O_4$	good thermal stability (up to 1273 K)	[93]
	$(Gd_{1/4}Eu_{1/4}Sm_{1/4}Nd_{1/4})_2Zr_2O_7$	single-phase pyrochlore structure	[94]
	$(Gd_{1/5}Eu_{1/5}Sm_{1/5}Nd_{1/5}La_{1/5})_2Zr_2O_7$		
	$(Gd_{1/6}Eu_{1/6}Sm_{1/6}Nd_{1/6}La_{1/6}Dy_{1/6})_2Zr_2O_7$		
	$(Gd_{1/7}Eu_{1/7}Sm_{1/7}Nd_{1/7}La_{1/7}Dy_{1/7}Ho_{1/7})_2Zr_2O_7$		
	$(Yb_{0.25}Y_{0.25}Lu_{0.25}Er_{0.25})_2SiO_5$	excellent phase stability and anisotropy in thermal expansion	[97]
	$Ba_{1.00}Fe_{5.83}Al_{1.19}Ti_{1.08}Cr_{1.12}Cu_{0.78}Ga_{1.03}In_{0.97}O_{19}$	single phase material with magnetoplumbite structure	[98]
	$(Co,Cr,Fe,Mn,Ni)_3O_4$, $(Co,Cr,Fe,Mg,Mn)_3O_4$, $(Cr,Fe,Mg,Mn,Ni)_3O_4$	high total conductivity at high temperatures; high absolute values of Seebeck coefficient.	[86]
Reactive flash sintering method	$Sr(Ti_{0.2}Y_{0.2}Zr_{0.2}Sn_{0.2}Hf_{0.2})O_{3-x}$	formation of single-phase oxides after sintering for 1 min	[105]
	$(Bi_{0.2}Na_{0.2}K_{0.2}Ba_{0.2}Ca_{0.2})TiO_3$	stable perovskite structure even in the presence of excessive Na^+ and K^+ ions	[106]
	$(MgCoNiCuZn)_{1-x}Li_xO$	charge compensation by the generation of oxygen vacancies	[107]
Spark plasma sintering	$A_6B_2O_{17}$ (A = Hf, Zr; B = Ta, Nb)	good hardness and fracture toughness; high temperature thermal stability	[169]
	$Sr((Zr_{0.94}Y_{0.06})_{0.2}Sn_{0.2}Ti_{0.2}Hf_{0.2}Mn_{0.2})O_{3-x}$	high density	[115]
Co-precipitation method	(Mg, Co, Ni, Cu, Zn)O	excellent sinterability	[170]
	$Ce_{0.2}Zr_{0.2}Y_{0.2}Gd_{0.2}La_{0.2}O_{2-\delta}$	small porosity	[171]
	$(Zn,Fe,Ni,Mg,Cd)Fe_2O_4$	average crystallite size 11.8 nm; microwave absorption properties	[121]
	$(La_{0.2}Ce_{0.2}Nd_{0.2}Sm_{0.2}Eu_{0.2})_2Zr_2O_7$	low thermal conductivity	[10]
Solvothermal synthesis	$FeCoNiMgCr(OH)(OCH_3)$	optimized OER performance	[128]
	$(FeCoNi_2CrMn)_3O_4$	large active surface area profiting from the nano structure	[130]
Solution combustion synthesis	$(Co_{0.2}Cu_{0.2}Mg_{0.2}Ni_{0.2}Zn_{0.2})O$	long-range antiferromagnetic behavior below Néel temperature	[35]
	(CoMnNiFeCr)O	high permittivity; low leakage current density	[172]
Sol-gel self-combustion	$PrBa_{0.5}Sr_{0.5}Co_{1.5}Fe_{0.5}O_{5.84-\delta}F_{0.16}$	enhanced P-ORR	[173]
	$SrFe_{0.25}Ti_{0.25}Co_{0.25}Mn_{0.25}O_{3-\delta}$	good chemical stability towards CO_2	[150]
Nebulized spray pyrolysis	$(Mn_{0.2}Fe_{0.2}Ni_{0.2}Mg_{0.2}Zn_{0.2})_3O_4$	good electrocatalytic properties	[174]
	$(Gd_{0.2}La_{0.2}Nd_{0.2}Sm_{0.2}Y_{0.2})_{1-x}Ca_xFeO_3$	single orthorhombic structure	[175]
Flame Spray Pyrolysis	$(Mn,Fe,Ni,Cu,Zn)_3O_4$	single spinel phase	[176]
Reactive sputtering	$(Al,Cr,Nb,Ta,Ti)O_2$	single rutile phase	[165]

procedure to achieve microscopic elemental diffusion. For the sintering process, the choice of a muffle furnace or a tube furnace depends on the desired atmospheric conditions [74,99,93,91,100,101]. Li et al. [61] effectively synthesized a HEOC with pyrochlore structure-$(La_{0.2}Nd_{0.2}Sm_{0.2}Eu_{0.2}Gd_{0.2})_2Zr_2O_7$ utilizing an SSR. Even at a temperature of 1200 °C, the thermal conductivity of this oxide remains below 1 $W{\cdot}m^{-1}{\cdot}K^{-1}$.

The advantages of SSR are low cost, simple process and treatment, and high tolerance for the precursors required for the reaction [102]. The main problems with this reaction method are the slow reaction rate (usually taking several hours) and high energy consumption [103].

Reactive flash sintering (RFS)

RFS, as depicted in Fig. 11b, denotes a synthesis method wherein the sample is subjected to simultaneous application of an electric field and heating conditions. As the electric field reaches a specific threshold, the current flowing through the sample experiences a rapid increase, triggered by thermal runaway. Concurrently, the sample undergoes rapid densification, accompanied by a pronounced luminescent phenomenon. The temperature at which the rapid current rise occurs is referred to as the critical temperature, typically lower than that required for conventional sintering [105]. This technique has been harnessed for the synthesis of HEOCs, demonstrating its ability to promote cation diffusion and expedite the formation of ideal HEOC configurations within a short span of time [105–107]. Wang et al. [105] successfully synthesized $Sr(Ti_{0.2}Y_{0.2}Zr_{0.2}Sn_{0.2}Hf_{0.2})O_{3-x}$ through the RFS technique, reducing the reaction time from 10 h, as required by traditional sintering processes, to a mere 1 min.

The main advantages of RFS are high reaction rates and low energy consumption. It does not rely on external heat sources but relies on current to heat the sample. This process is prone to difficulty in obtaining a uniform microstructure due to poor thermal management [108].

Spark plasma sintering (SPS)

SPS, commonly known as field-assisted sintering technology, represents a synthesis technique that employs a low voltage, DC pulse current, and a pressure-assisted system to sinter samples [110,111]. The advantages of SPS are quite evident. Throughout the sintering process, the sample is uniformly heated at a

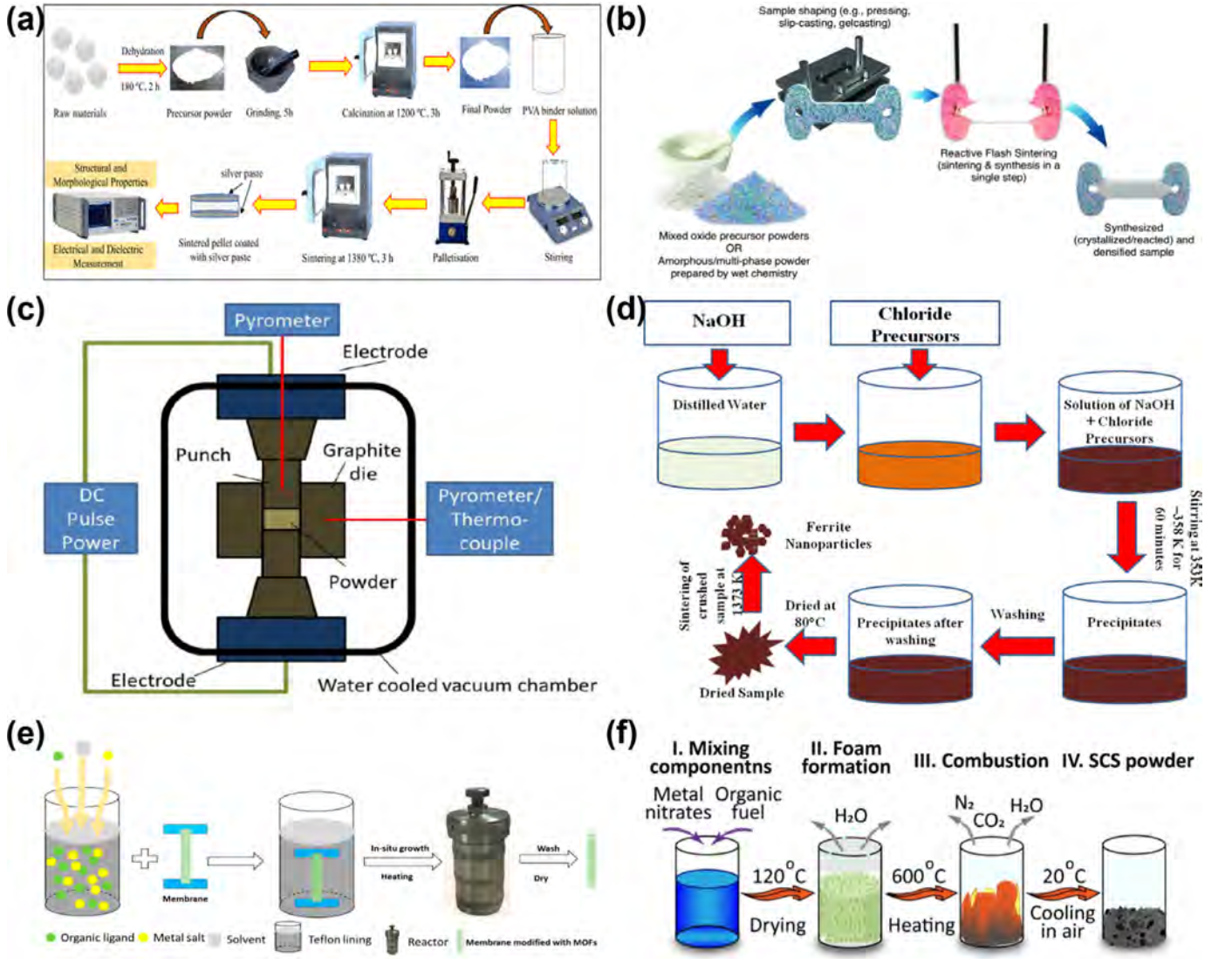

FIG. 11

(a) The steps of SSR for the synthesis of BCZT-based ceramic samples [104]; (b) Schematic diagram of RFS showing the sintering process of dog-bone samples [109]; (c) Structure diagram of SPS device[110]; (d) Schematic showing the preparation of ferrite by CP [124]; (e) Schematic showing solvothermal synthesis of MOF-based films [133]; (f) Schematic showing the main steps of SC [145].

rapid rate, facilitating the production of high-density materials [112,113]. The overall operation of the system is illustrated in Fig. 11c [110]. The sintering process achieves an impressive heating rate of up to 1000 °C·min^{-1}, significantly reducing the overall duration of the sintering process. In standard mode, the cooling rate can reach 150 °C·min^{-1}, and this rate can be further enhanced to 400 °C·min^{-1} with the inclusion of active cooling [114]. Mattia Biesuz et al. [115] successfully synthesized HEOC – $Sr((Zr_{0.94}Y_{0.06})_{0.2}Sn_{0.2}Ti_{0.2}Hf_{0.2}Mn_{0.2})O_{3-x}$ using the SPS technique. This work presents novel insights into the preparation method of HEOCs.

The benefits of SPS technology encompass rapid heating rates, reduced sintering durations, precise control over microstructural formation, energy efficiency, and environmental friendliness [116]. In contrast to conventional sintering techniques, SPS enables high-quality sintering to be achieved at lower temperatures [117]. Notably, this method imposes stringent atmospheric conditions during the sintering process. Nevertheless, challenges persist in the fabrication of large-scale materials using this approach [118].

Co-precipitation (CP)

The CP method, as illustrated in Fig. 11d, holds significant importance as a chemical synthesis approach widely employed in the production of diverse metal oxide nano powder materials [119]. This method offers the distinct advantage of directly synthesizing nano-powder materials with a homogeneous chemical composition through solution-based reactions. Notably, it is characterized by its simplicity, affordability, and versatility. To generate nano-powders using this method, precise regulation of various process conditions is essential, including component ratio, reactant concentration, temperature, dispersant, mixing technique, pH value, washing method, drying temperature, and methodology. By meticulously controlling these process

conditions, one can effectively influence the particle size, morphology, crystal structure, as well as the physical and chemical characteristics of the nano powders. Furthermore, the CP method can be synergistically combined with other chemical synthesis techniques such as hydrothermal and sol–gel methods to produce nano powder materials with distinct morphology and structure, thereby expanding the scope and efficacy of this technique [120]. Radoń et al. [121] successfully synthesized (Zn, Fe, Ni, Mg, Cd) Fe_2O_4 utilizing the CP method. The resulting sample exhibit a microscopic grain size of 11.8 nm. Experimental findings confirm that samples with a thickness of 0.8–1 cm displayed the highest absorption rate for microwaves near 2 GHz.

The CP technique offers operational simplicity and controllability, facilitating the simultaneous preparation of a substantial quantity of sample particles with high efficiency [122]. Through manipulation of various parameters such as reactant concentration, temperature, and pH levels, the morphology of the resultant product can be finely tuned during the synthesis process. However, the crystallization rate, which is influenced by the reactants, presents a limitation to this method. Certain reactants release ions that impede the formation of co-precipitates, thereby impacting the reaction dynamics. Consequently, the stability of the final product is compromised, rendering it susceptible to environmental influences [123].

Solvothermal synthesis

The solvothermal method, as depicted in Fig. 11e, represents a synthesis technique grounded in the crystallization process of substances [125]. The primary principle of this method involves utilizing organic solvents as the reaction medium to produce functional materials of exceptional quality and purity. This process is typically conducted within a sealed autoclave reactor. The solvothermal method offers numerous advantages, including straightforward reaction equipment, a simplified preparation process, low reaction temperatures, and the ability to generate particles of small sizes [126]. Notably, this method also enables the control of product morphology and particle size, owing to the adjustability of reaction conditions such as temperature, pH, reactant concentration, and the addition of surfactants. By effectively manipulating these parameters, the morphology, particle size, and ultimately, the performance of the resulting product can be precisely regulated [127]. Furthermore, the application of the solvothermal method expands to encompass the synthesis of various functional materials, including nanostructured materials, porous materials, photocatalytic materials, biomaterials, and more. In recent years, the solvothermal method also finds extensive use in the preparation of HEOCs. This technique allows for the production of high-quality, high-purity HEOCs, with a certain degree of control over their microstructure and physical properties, thereby bolstering their applicability [128–130]. Wang et al. [130] successfully employed the solvothermal method to synthesize HEOC—$(FeCoNi_2CrMn)_3O_4$. The utilization of solvothermal methods imparts nanostructures to HEOCs, thereby enabling their application in catalysis.

Due to the confinement of the solvothermal reaction within a sealed vessel, direct observation of the reaction process is hindered, limiting access solely to the outcome of the reaction rather than the process itself [131]. This constraint poses challenges to elucidating the underlying reaction mechanism and hinders comprehensive investigation into the intricacies of the reaction pathway [132].

Solution combustion (SC)

The method, SC, employed for synthesizing oxides involves the preparation of a sol by combining metal nitrates, glycine, and water. Subsequently, the mixture is dried to form a gel, which is then subjected to high temperatures to yield HEOCs, as depicted in Fig. 11f [134–139]. One notable advantage of this method lies in its efficiency in terms of time and energy, as the combustion reaction is a rapid chemical process capable of producing high-purity oxides within a short timeframe. Furthermore, the equipment required for this method is simple and cost-effective, eliminating the need for expensive autoclaves or other intricate experimental apparatus [140]. Another significant advantage is its applicability to a wide range of ceramic materials, including oxides, carbides, borides, and more [141]. Additionally, this method enables the synthesis of high-purity complex oxides, as metal nitrates are typically highly soluble in water and can be easily removed from the reaction mixture [135]. Moreover, by controlling the combustion temperature, this method can generate metastable phases in a shortened time, which exhibit favorable physical and chemical properties, thereby showcasing potential advantages in specific applications [142]. Mao et al. [35] successfully prepared HEOC nanocrystalline powder—$(Co_{0.2}Cu_{0.2}Mg_{0.2}Ni_{0.2}Zn_{0.2})O$ through the solution combustion method, which exhibit antiferromagnetic behavior below the Néel temperature.

Given the intrinsic nature of the combustion process as a self-sustaining and spontaneous reaction, external energy inputs become superfluous once the reaction initiates, leading to a lack of control over the reaction dynamics [143]. This inherent characteristic complicates the regulation and manipulation of the SC process, posing challenges in directing and modulating the reaction trajectory [144].

Sol-gel self-combustion (SGSC)

The SGSC method (Fig. 12a) is a promising approach for synthesizing oxides through a combustion reaction, which represents a novel synthetic strategy combining the sol–gel and SC method [146]. Typically, metal nitrates are employed as oxidizing agents, while citric acid serves as both a complexing agent and fuel. Citric acid plays a crucial role as a complexing agent as it can form stable complexes with metal ions, thereby facilitating the reaction [147]. Concurrently, it acts as a fuel to provide the energy required for the reaction. Compared to the conventional combustion method, the SGSC method boasts remarkable advantages such as a fast reaction rate, low reaction temperature, and high purity of the synthesized products [148]. Moreover, this method exhibits excellent controllability, allowing for the adjustment of the morphology, size, and crystal structure of the product by tuning the reaction conditions. By manipulating the reaction parameters such as the reaction temperature, reaction time, and reaction atmosphere, it is possible to control the microstructure and properties of the product [138,149]. Therefore, the SGSC method holds great promise for the preparation

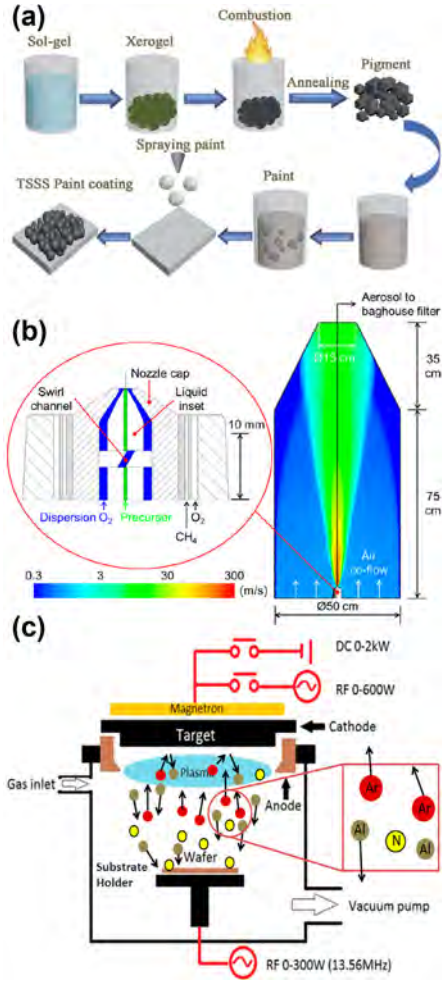

FIG. 12

(a) Schematic showing the SGSC preparation process [151]; (b) Schematic diagram of the geometric structure of the FSP two-phase atomizer [159]; (c) Schematic showing the preparation of AlN thin films by RS [168].

of HEOs. Shen et al. [150] used the SGSC method to prepare perovskite $SrFe_{0.25}Ti_{0.25}Co_{0.25}Mn_{0.25}O_{3-\delta}$, which was employed in the cathode of solid oxide fuel cells with suppressed surface strontium segregation.

The SGSC method entails the precise selection of complexing agents and metal ions to generate complexes, which can potentially impose constraints on particular reactants [147].

Spray pyrolysis (SP)

The SP method can be divided into two categories: nebulizing spray pyrolysis (NSP) and flame spray pyrolysis (FSP). NSP is a commonly employed chemical method for producing deposited thin film oxides. The fundamental principle of this method involves nebulizing an elemental salt using ultrasonic waves and subsequently subjecting it to high-temperature pyrolysis to convert it into an oxide. During this process, a salt solution and oxygen are mixed and flow into a hot-wall reactor, where pyrolysis reactions occur at elevated temperatures. Following the pyrolysis reaction, the produced oxides are collected by a filter-based collector and compressed into thin films. These films are then sintered through heat treatment to form deposited oxide films possessing desirable physical and chemical properties [38].

This method can be utilized to produce various HEOCs, such as $(Co_{0.2}Cu_{0.2}Mg_{0.2}Ni_{0.2}Zn_{0.2})O$ [38], $(Ce_{0.2}La_{0.2}Pr_{0.2}Sm_{0.2}Y_{0.2})O_{2-\delta}$ [152], $Li(NiCoMnAlZn)O_2$ [153], and others. By controlling reaction conditions such as oxygen pressure and temperature, the reaction rate and oxygen concentration can be adjusted to precisely manipulate the physical and chemical properties of the resulting product. Furthermore, this method offers the advantages of high efficiency, simplicity, and facile scalability [154].

On the other hand, FSP is a widely utilized method in the synthesis of various oxide nano powders [155]. The basic principle of this method involves injecting liquid metal and oxidizing gas into the flame zone, where a chemical reaction occurs, yielding metal oxide nano powders [155–157]. These products can be simple oxides or composite oxides, such as $(Co_{0.2}Cu_{0.2}Mg_{0.2}Ni_{0.2}Zn_{0.2})O$ [37] and (Co, Cu, Mg, Ni, Zn)O [126], along with other HEOCs. The process setup typically includes sections for reactant delivery, flame and reaction chambers, collection systems, and a vacuum device [158]. In this process, the reactants are delivered to the reaction chamber through the delivery part and then injected into the flame zone alongside the oxidizing gas. Within the flame zone, the reactants undergo chemical reactions, resulting in the formation of oxide nano powders, which are subsequently collected in the collection system [158,159]. Fig. 12b illustrates the geometric structure of an FSP two-phase atomizer [159]. Compared to other liquid-phase synthesis methods, FSP boasts several advantages. Firstly, it exhibits a short reaction time, typically ranging from a few seconds to a few minutes. Secondly, the produced product displays greater homogeneity, higher crystalline quality, and a narrower particle size distribution. Additionally, the particle size and structure of the product can be relatively easily controlled by adjusting processing conditions such as reaction temperature, flame zone location, reactant concentration, and more [155].

SP emerges as a continuous, swift, and adjustable technique devoid of the ultra-high vacuum demands inherent in gas-phase methodologies. It allows for control over particle size and morphology of the resulting product, ensuring high purity and uniform component distribution [160]. Nevertheless, the stringent requirements for precursor material preparation and the necessity for selecting suitable solvents aligned with subsequent process conditions present notable considerations [161].

Reactive sputtering (RS)

RS, as depicted in Fig. 12c, is a sputter deposition technique specifically designed for the precise deposition of thin films with varying compositions onto designated substrates. This method leverages the chemical reaction between sputtered particles originating from the target material and introduced reactive gases, such as oxygen or nitrogen, to produce oxide and nitride films, respectively [162]. The introduction of reactive gases significantly influences the deposition process, necessitating the careful control of the partial pressures of both working and reactive gases to mitigate hysteresis behavior. In general, most reaction-based sputtering processes exhibit hysteresis-like behavior, underscoring the importance of fine-tuning parameters, includ-

ing the partial pressures of working (or noble) and reactive gases [163].

A critical model, known as the Berg model, is introduced by Berg et al. to estimate the impact of incorporating reactive gases during sputtering. This model proves invaluable in gauging the influence of relative pressure and gas flow rates on target erosion and the deposition rate of thin films onto desired substrates. By manipulating the relative pressures of gases, the film's composition can be precisely controlled, thereby optimizing its properties [164]. In a relevant application, Kirnbauer et al. [165] employed the RS method to craft HEO thin films—(Al,Cr,Nb,Ta,Ti)O_2. These films exhibit greater hardness compared to traditional ternary oxides.

The film sample fabricated via RS showcases notable attributes such as elevated purity levels and adjustable properties [166]. Nonetheless, a challenge arises during the production of dielectric or insulating material compound films, characterized by a hysteresis effect. This effect manifests as a correlation between the sputtering rate and the flow rate of reactive gases. Consequently, the presence of this phenomenon limits the achievable stoichiometric ratios of compounds through reactive sputtering techniques [167].

Properties and applications

Ceramic oxides possess diverse properties, rendering them valuable as functional materials across numerous fields. HEOCs, benefiting from the cocktail effect, open expansive avenues for development. Functional ceramics within high-entropy systems exhibit a higher degree of disordered crystal structures in contrast to their low-entropy counterparts. The critical role of crystal structure in high-entropy oxide ceramics serves as a unique platform for controlling a diverse range of mechanical [182], electrical [181], and thermal properties [170] and applications. For example, variations in crystal symmetry, lattice parameters, and coordination environments influence factors such as hardness, thermal conductivity, and dielectric constant. By tailoring the composition and crystal structure, researchers can design materials with specific properties optimized for various applications, including structural components, electronic devices, and thermal barrier coatings. Ferroelectric HEOCs commonly display reduced coercive electric field and residual polarization, thereby offering promising research opportunities in the realm of energy storage applications for ceramic materials [177]. Table 2 provides an overview of HEOCs featuring various structures and their primary performance. Research areas of interest for the rock salt structure encompass ionic conductivity [178], catalysis [179], magnetic properties [180], electrical properties [181], thermal properties [170], and mechanical properties [182]. Thermal [171] and mechanical [183] properties take precedence in the study of the fluorite structure. Investigations into perovskite structures primarily target electrical properties [184], magnetic properties [185], thermal properties [186], ionic conductivity [187], and catalytic effects [188]. Apart from the properties mentioned above, the spinel structure is mainly associated with magnetic properties [189–191] while the pyrochlore structure has been extensively explored in terms of mechanical [192] and thermal properties [10]. In this section, we provide a summary of the varied properties of HEOCs and offer insights into their prospective application areas.

Thermal conductivity

Thermal conductivity is a measure of a material's ability to conduct heat. Ceramics with low thermal conductivity are commonly used to protect surfaces in high-temperature systems. Thermal barrier coating ceramics have properties such as low thermal conductivity, high thermal stability, and compatibility with the substrate (Table 3). The decrease in thermal conductivity observed in high-entropy compounds is due to the scattering effect of phonons caused by the presence of multiple components and lattice distortion [63]. Fig. 13 provides a summary of the thermal conductivity and density of selected high-entropy compounds.

Maiti et al. [83] fabricated a perovskite HEOC, Sr($Ti_{0.2}Fe_{0.2}$-$Mo_{0.2}Nb_{0.2}Cr_{0.2}$)O_3. By incorporating transition metal elements into the B-site of $SrTiO_3$, high-entropy oxide ceramics with significantly reduced thermal conductivity are intentionally designed. Remarkably, the thermal conductivity of Sr($Ti_{0.2}Fe_{0.2}$-$Mo_{0.2}Nb_{0.2}Cr_{0.2}$)O_3 is as low as 0.7 $W{\cdot}m^{-1}{\cdot}K^{-1}$ at 1100 K.

Liu et al. [193] developed a new variant of high-entropy zirconate, denoted as ($Sm_{0.2}Eu_{0.2}Tb_{0.2}Dy_{0.2}Lu_{0.2}$)$_2Zr_2O_7$. Remarkably, this material showcases an extremely low thermal conductivity of 0.031 $W{\cdot}m^{-1}{\cdot}K^{-1}$ after undergoing high-temperature heat treatment. Advanced characterization methods, including scanning electron microscopy, have provided evidence of the material's internal nano porous structure.

In a study by Wright et al. [63], the relationship between thermal conductivity and structural parameters of 22 entropy-stabilized single-phase pyrochlores is investigated. After comparing various parameters, it is found that disorder within the unit cell parameters shows the strongest correlation with changes in thermal conductivity. Lattice distortion was found to have a significant influence on the thermal conductivity of high-entropy compounds.

TABLE 2

Summary of properties and structures of HEOCs.

	Rock-salt	Fluorite	Perovskite	Spinel	Pyrochlore
Ion conductivity	√		√	√	
Catalysis	√		√	√	
Magnetic property	√		√	√	
Electrical property	√		√	√	
Thermal property	√	√	√	√	√
Mechanical property	√	√		√	√

TABLE 3

Summary of thermal conductivity of HEOCs.

Materials	Key Findings	Ref
$Mg_xNi_xCu_xCo_xZn_xSb_xO$, x = 0.167	1.41 ± 0.17 $W{\cdot}m^{-1}{\cdot}K^{-1}$	[194]
$(Ce_{0.2}Zr_{0.2}Hf_{0.2}Sn_{0.2}Ti_{0.2})O_2$	1.28 $W{\cdot}m^{-1}{\cdot}K^{-1}$	[44]
$(Sm_{1/4}Eu_{1/4}Gd_{1/4}Yb_{1/4})_2(Ti_{1/2}Hf_{1/4}Zr_{1/4})_2O_7$	1.36 ± 0.04 $W{\cdot}m^{-1}{\cdot}K^{-1}$	[63]
$(Hf_{0.25}Zr_{0.25}Ce_{0.25})(Y_{0.125}Ca_{0.125})O_{2-\delta}$	1.10 ± 0.20 $W{\cdot}m^{-1}{\cdot}K^{-1}$	[42]
$(Hf_{0.284}Zr_{0.284}Ce_{0.284}Y_{0.074}Ca_{0.074})O_{2-\delta}$	1.54 ± 0.05 $W{\cdot}m^{-1}{\cdot}K^{-1}$	[183]
$(Dy_{0.2}Ho_{0.2}Er_{0.2}Y_{0.2}Yb_{0.2})_3NbO_7$	0.724 $W{\cdot}m^{-1}{\cdot}K^{-1}$	[195]
$(La_{0.2}Ce_{0.2}Nd_{0.2}Sm_{0.2}Eu_{0.2})_2Zr_2O_7$	0.76 $W{\cdot}m^{-1}{\cdot}K^{-1}$	[10]

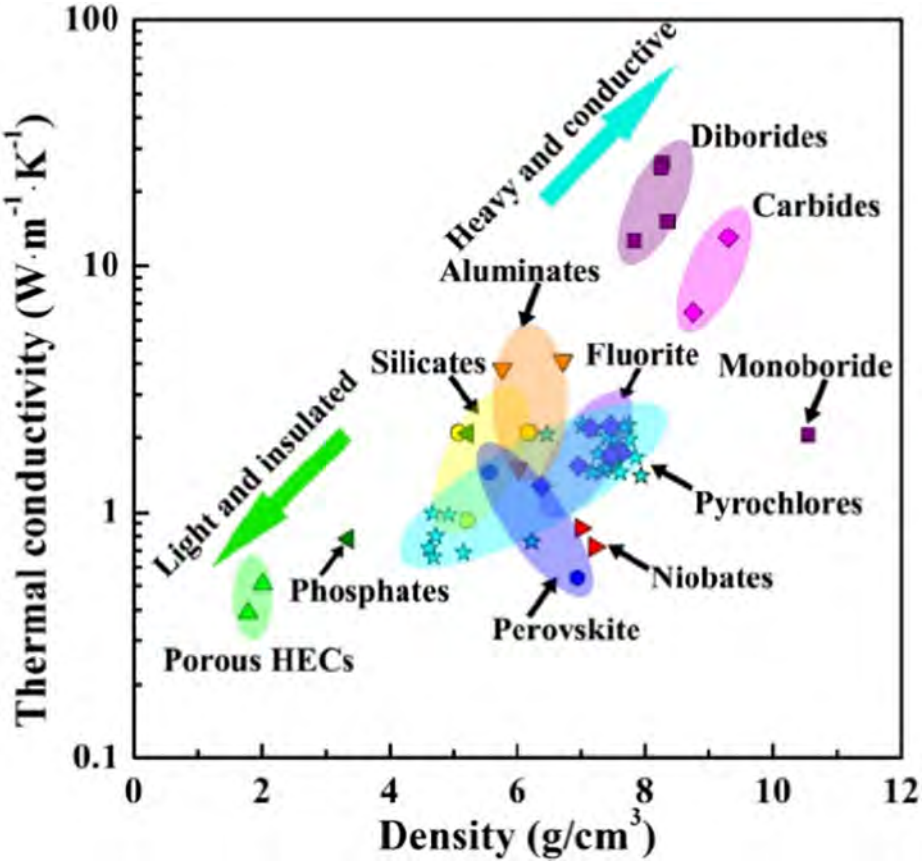

FIG. 13

The relationship between thermal conductivity and density of some high-entropy compounds is summarized [21].

Catalytic performance

Catalysis is a crucial and intricate process in the chemical industry. Researchers are constantly striving to discover new catalysts with high performance. In this regard, HEOCs have shown great potential in catalysis. These ceramic materials possess unique chemical bonding patterns, which offer promising opportunities for catalytic reactions [196,197]. HEOCs not only exhibit high activity, selectivity, and long-term stability, but they also have controllable costs, making them suitable for the production of affordable high-performance catalysts (Table 4).

HEOCs can play a significant role not only as catalysts themselves but also as catalyst supports. By tuning the geometry and pore structure of HEOCs, their surface area and catalytic performance can be further enhanced. Recent research efforts have focused on noble metal-supported HEOCs, such as (MgCoNiCuZn)O, for CO oxidation [40] and CO_2 hydrogenation reactions [179]. Disordered oxides can promote the high dispersion of noble metal catalysts, like Pt/Ru, enhance their activity, and provide resistance to high-temperature processing.

In the CO oxidation reaction, HEOCs have demonstrated the ability to achieve high conversion rates at low temperatures and exhibit good reusability. For instance, a catalyst loaded with 5 wt % Pt/Ru showed CO production and CO2 conversion exceeding 45 % at 500 °C. Furthermore, the CO selectivity of the CO2 hydrogenation catalyst surpassed 95 % [179].As the properties of HEOCs are further studied and optimized, they are expected to bring about more innovations and breakthroughs in the field of catalysis.

TABLE 4

Summary of catalytic properties of HEOCs.

Materials	Key Findings	Ref.
$(Co_{0.2}Cu_{0.2}Mg_{0.2}Ni_{0.2}Zn_{0.2})O$	enhanced the rate of the redox reaction	[198]
$(CeZrHfTiLa)O_x$	increased activity for CO oxidation at lower temperatures	[199]
$Ru_{0.13}/Ba_{0.3}Sr_{0.3}Bi_{0.4}(Zr_{0.2}Hf_{0.2}Ti_{0.2}Fe_{0.27})O_3$	51 % CO conversion at 90 °C within time of less than 1 s	[188]
$TiZrHfNbTaO_{11}$	higher light absorbance compared to all binary oxides and successful hydrogen production	[82]
(NiMgCuZnCo)O-CuCeOx	enhanced thermal stability for the oxidation of CO at elevated temperatures.	[200]
$La_{0.2}Pr_{0.2}Sm_{0.2}Sr_{0.2}Ca_{0.2}Fe_{0.9}Ni_{0.1}O_{3-\delta}$	CO production rate is 1.04–4.06 ml•min^{-1}, from 1.2 V-1.8 V.	[10]

Ionic conductivity and capacity of battery

HEOCs have gained considerable attention in the field of Li-ion batteries (Table 5). These materials are particularly suitable for use as anode materials due to their high ionic conductivity characteristics [99]. One specific HEOC material, (MgCoNiCuZn)O, attracts the interest of researchers because of its strong ionic conductivity and cycle stability as an anode material [37,38,198,201]. It should be noted that the HEOCs used in the charging mechanism of Li-ion batteries require a complex process of reducing transition metal cations [37,178].

Researchers are constantly working to improve the structure and composition of HEOCs in order to enhance their lithium-ion conductivity and cycling stability. They achieve this by carefully controlling the crystal structure, lattice defects, and ion diffusion pathways of HEOCs [201]. Techniques such as interface engineering and nanoscale optimization are frequently employed to improve the performance of HEOCs in Li-ion batteries [36].

Nanoscale management is a key approach to enhancing the functionality of HEOCs. By adjusting factors such as particle size, shape, and crystallinity, it is possible to increase the surface area and ion diffusion pathways, leading to faster ion transport rates [37,201]. Additionally, nanoscale management is effective in reducing volume expansion and structural degradation during extended cycling, resulting in longer battery life [99,187].

The research and optimization efforts mentioned above make HEOCs highly promising for use in lithium-ion batteries. This progress has the potential to provide more reliable and efficient energy solutions in industries such as electric vehicles, portable electronics, and renewable energy storage. It is expected that HEOCs will continue to expand and be more widely used in sustainable energy storage as future research advances [9].

Magnetic property

HEO materials have been under consistent manufacturing and investigation in recent years, yet their magnetic properties have only recently emerged as a focal point. The magnetic characteristics of oxides are influenced by their chemical composition, physical structure, and spintronic states. The magnetic evaluation of HEOs is particularly intricate due to lattice anisotropy, intrinsic chemical disorder, structural intricacies, and the random arrangement of magnetic atoms, each possessing varied electronic and ionic configurations [207,208]. Owing to the multitude of nearby ion configurations within HEOs, they give rise to intricate magnetoelectronic free energy conditions, ultimately stabilizing novel spintronic states [209]. Table 6 provides a summary of research pertaining to the magnetic properties of HEOCs.

Meisenheimer et al. [210] studied the disorder and anisotropy of permalloy/$(Mg_{0.25(1-x)}Co_xNi_{0.25(1-x)}Cu_{0.25(1-x)}Zn_{0.25}$

TABLE 5

Summary of properties for battery applications of HEOCs.

Materials	Key Findings	Ref.
$(MgCoNiCuZn)_{1-x-y}Ga_yA_xO$ (A refers to Li, Na and K)	Li^+ conductivity (>10^{-3} S·cm^{-1}), Na^+ conductivity (5×10^{-6} S·cm^{-1})	[36]
$(MgCoNiCuZn)_{1-x}Li_xO$	1 mS·cm^{-1} at room temperature and 20 mS·cm^{-1} at 100 °C	[202]
$(Mg_{0.2}Ti_{0.2}Zn_{0.2}Cu_{0.2}Fe_{0.2})_3O_4$	Reversible capacity of 504 mA h·g^{-1}	[99]
$(Bi,Na)_{0.2}(La,Li)_{0.2}(Ce,K)_{0.2}Ca_{0.2}Sr_{0.2}]TiO_3$	Anode material with initial discharge capacity of 125.9 mA h·g^{-1}	[187]
$BaCe_{0.5}Zr_{0.2}Y_{0.1}Yb_{0.1}Gd_{0.1}O_{3-\delta}$	Total conductivity 1×10^{-2} S cm^{-1} in wet air at 600 °C	[203]
$BaSn_{0.16}Zr_{0.24}Ce_{0.35}Y_{0.1}Yb_{0.1}Dy_{0.05}O_{3-\delta}$	Protonic conductivity 8.3 mS cm^{-1} in humidified air (3 % H2O) at 600 °C	[204]
$La_{0.2}Pr_{0.2}Nd_{0.2}Sm_{0.2}Ba_{0.1}Sr_{0.1}Co_{0.2}Fe_{0.6}Ni_{0.1}Cu_{0.1}O_{3-\delta}$	Electrical conductivity 635.15 S·cm^{-1} at 800 °C	[205]
$Pr_{1/6}La_{1/6}Nd_{1/6}Ba_{1/6}Sr_{1/6}Ca_{1/6}CoO_{3-\delta}$	Electrical conductivity > 1000 S·cm^{-1} at 300–750 °C	[206]

TABLE 6

Summary of magnetic property of HEOCs.

Materials	Key Findings	Ref.
$(Mg_{0.2}Co_{0.2}Ni_{0.2}Cu_{0.2}Zn_{0.2})O$	slow magnetic transformation, long-range ordered antiferromagnetic ground state	[211]
$Mg_{0.2}Co_{0.2}Ni_{0.2}Cu_{0.2}Zn_{0.2}O$	long-range magnetic ordering at temperatures below 120 K	[212]
$Mg_{0.2}Co_{0.2}Ni_{0.2}Cu_{0.2}Zn_{0.2}O$	Long-range ordered antiferromagnetic behavior below T_N = 106 K, paramagnetic behavior at room temperature.	[35]
$Y(Co_{0.2}Cr_{0.2}Fe_{0.2}Mn_{0.2}Ni_{0.2})O_3$, $La(Co_{0.2}Cr_{0.2}Fe_{0.2}Mn_{0.2}Ni_{0.2})O_3$,	ferromagnetic clusters within an antiferromagnetic matrix	[185]
$(Gd_{0.2}La_{0.2}Nd_{0.2}Sm_{0.2}Y_{0.2})CoO_3$, $(Gd_{0.2}La_{0.2}Nd_{0.2}Sm_{0.2}Y_{0.2})FeO_3$, $(Gd_{0.2}La_{0.2}Nd_{0.2}Sm_{0.2}Y_{0.2})CrO_3$	chemical disordering in rare-earth sites with specific magnetic features	[78]
$BaFe_{5.83}Al_{1.19}Ti_{1.08}Cr_{1.12}Cu_{0.78}Ga_{1.03}In_{0.97}O_{19}$	ferromagnetic at low temperatures, paramagnetic at room temperature	[98]
$(Al_{1/6}Co_{1/6}Cr_{1/6}Fe_{1/6}Mn_{1/6}Ni_{1/6})_3O_4$	long-range ferromagnetic behavior below Curie temperature of 248 K	[213]
$(Cr_{0.2}Fe_{0.2}Mn_{0.2}Co_{0.2}Ni_{0.2})_3O_4$, $(Cr_{0.2}Fe_{0.2}Mn_{0.2}Ni_{0.2}Zn_{0.2})_3O_4$, $(Cr_{0.2}Fe_{0.2}Mn_{0.2}Co_{0.2}Zn_{0.2)3}O_4$	replacement of Co^{2+} or Ni^{2+} as nonmagnetic ion attenuates ferromagnetic ordering and magnetic moments	[214]

$_{(1-x)}$)O heterostructures. The presence of anisotropic magnetic exchange and critical blocking temperature suggests that entropy-stable oxides possess antiferromagnetic properties. By changing the composition of the oxide, the disorder, exchange field and magnetic anisotropy can be tuned. Taking advantage of this tunability, they successfully increase the strength of the exchange field at low temperatures by a factor of 10 compared to permalloy/CoO heterostructures. The structural and magnetic parameters of the crystals deviate significantly from the mixture rules, indicating that configurational entropy plays a dominant role in the crystals. These results demonstrate that the unique properties of entropy-stable materials can be exploited and tailored to engineer magnetic functional phenomena in oxide films.

Dielectric property

A crucial factor to consider when designing electronic devices, particularly energy storage capacitors, is the high dielectric constant (ε′). Traditionally, $BaTiO_3$ has been widely employed in capacitors. However, the introduction of the concept of high entropy has paved the way for a fresh approach to developing high-performance dielectric materials. Earlier studies revealed a connection between grain size and dielectric properties [215]. As research has progressed, it has become evident that HEOCs with a rock-salt structure exhibit a notably high ε′, and this performance can be fine-tuned by adjusting the elemental composition. These findings suggest a promising application of HEOCs in capacitance-based energy storage devices [66]. Research into the dielectric properties of HEOCs is not confined to the rock-salt structure, as researchers have also ventured into the development of other varieties of high-entropy dielectric materials.

Bérardan et al.[66] conducted research on heterovalent element substitution and dielectric properties of HEOC, (Mg,Ni,Co,Cu,Zn)O. Through experiments, it is found that HEOCs are highly tolerant of elements in the + 1 valence state. The substitution ratio of Li element in HEOCs can be as high as 16.6 %. Among them, $(Mg,Ni,Co,Cu,Zn)_{0.95}Li_{0.05}O$ has a ε′ as high as $2*10^5$ under the test conditions of 20 Hz and 440 K.

Zhou et al. [216] successfully prepared high-entropy perovskite oxide $Sr(Zr_{0.2}Sn_{0.2}Hf_{0.2}Ti_{0.2}Nb_{0.2})O_3$ (SZSHTN) and introduced it into $Na_{0.5}Bi_{0.5}TiO_3$ (NBT). Through research, it was found that the 0.8NBT–0.2SZSHTN system has the best performance. The ε′ of this component is as high as 2000 at 150 °C with low dielectric loss (tanδ). The relevant studies are summarized in Table 7.

Piezoelectric property

Piezoelectric materials [221,222] are special materials that generate an electrical potential in response to applied mechanical stress, or mechanical motion or deformation when subjected to an electric field [223,224]. This characteristic makes piezoelectric materials widely used in electromechanical fields such as sensors, actuators, and transducers [225–227]. The occurrence of piezoelectricity depends on the crystal structure and the direction of

TABLE 7

Summary of dielectric property of HEOCs.

Materials	Key Findings	Ref.
$Sr(Zr_{0.2}Sn_{0.2}Hf_{0.2}Ti_{0.2}Nb_{0.2})O_3$ (SZSHTN)	high ε′ > 2000 at 150 °C and low tanδ (<0.01, 90–341 °C)	[216]
$0.8Na_{0.5}Bi_{0.5}TiO_3$–0.2SZSHTN		
$Ba(Zr_{0.2}Ti_{0.2}Sn_{0.2}Hf_{0.2}Me_{0.2})O_3$ (Me = Nb^{5+}, Ta^{5+})	low tanδ at 20 Hz – 2 MHz (<0.002)	[81]
$(NaBaBi)_x(SrCa)_{(1-3x)/2}TiO_3$ (x = 0.205)	ε′ ~ 4920	[79]
$Sr_{0.9}La_{0.1}MeO_3$ (Me = Zr, Sn, Ti, Hf, Mn, Nb)	$\varepsilon_r/\varepsilon_{25°C}$ < 5 % within – 100 to 300 °C	[217]
$Y_{0.2}Eu_{0.2}Er_{0.2}Dy_{0.2}Lu_{0.2})_3(Al_xFe_{1-x})_5O_{12}$ (x = 0.4–0.6)	ε_r' decrease with increased Al content	[218]
$(FeCoCrMnZn)_3O_4$	ε′ decreases with increasing pressure	[219]
$(Bi_{0.2}Na_{0.2}K_{0.2}Ba_{0.2}Ca_{0.2})TiO3$	ε′ ~ 1200 at 240 °C	[106]
$Ba(Ti_{1/6}Sn_{1/6}Zr_{1/6}Hf_{1/6}Nb_{1/6}Ga_{1/6})O_3$	ε′ ~ 65 at 650 °C	[220]

applied stress [228,229]. For example, quartz becomes polarized when compressive stress is applied in the [100] direction, but not in the [001] direction [88]. This relationship between polarization and stress can be described by the piezoelectric coefficient (d_{33}). The high d_{33} is the key to achieving efficient energy conversion [230,231,125]. Many crystals containing tetrahedral groups, such as ZnO and ZnS, are piezoelectric because applied stress causes the tetrahedra to deform [88]. Lead zirconate titanate ($Pb(Zr,Ti)O_3$) is a typical piezoelectric material with a perovskite structure [100]. It is a composition of solid solution between $PbZrO_3$ and $PbTiO_3$. These solid solutions can exhibit antiferroelectric and ferroelectric behavior under certain compositions. Recently, a high-entropy design has been proposed to achieve high d_{33} values [232], which is a new strategy different from constructing morphotropic phase boundary (MPB) and polymorphic phase boundary (PPB) [8].

Liu et al. [230] prepared piezoelectric ceramic, $Pb(Ni_{0.173}In_{0.07}Zr_{0.034}Ti_{0.306}Nb_{0.417})O_3$, with ultrahigh $d_{33} \sim 1200$ pC/N through a high-entropy strategy. The results show that the multiple interactions between atoms in the A-site and B-site are due to the increase in the types of elements in the B-site and the increase in system entropy, which weakens the long-range polarization order and enhances the flexibility of the external field under the action of polarization. Table 8 summarizes high-entropy piezoelectric materials.

Ferroelectric property

Disorder has been a pivotal research area concerning ferroelectric materials due to its profound influence on the formation of homogeneous phases and the development and propagation of domain walls. When disorder is evenly dispersed throughout the lattice, it introduces a novel category of high-entropy ferroelectric materials, capable of uniquely impacting phase dynamics [73]. The composition of cations plays a decisive role in governing the properties of high-entropy ferroelectric materials. This mode of regulation offers fresh perspectives on several fundamental research questions. Disordered alterations within the lattice can exert significant influence over the metastability and Curie temperature of the crystalline phase [236]. Additionally, high-entropy strategies exhibit the potential to enhance ferroelectric properties, including the augmentation of ferroelectric polarization, the suppression of loss, and the fine-tuning of relaxor behaviour.

Liu et al. [51] prepared a series of high-entropy perovskite ceramics—$(Bi_{0.2}Na_{0.2}Ba_{0.2}Sr_{0.2}Ca_{0.2}TiO_3$, $Bi_{0.2}Li_{0.2}Ba_{0.2}Sr_{0.2}Pb_{0.2}TiO_3$, $Bi_{0.2}Na_{0.2}Ba_{0.2}Sr_{0.2}Pb_{0.2}TiO_3$, $Bi_{0.2}K_{0.2}Ba_{0.2}Sr_{0.2}Pb_{0.2}TiO_3$ and $Bi_{0.2}Ag_{0.2}Ba_{0.2}Sr_{0.2}Pb_{0.2}TiO_3$). It is found that $Bi_{0.2}Na_{0.2}Ba_{0.2}Sr_{0.2}Pb_{0.2}TiO_3$ high-entropy ferroelectrics achieved strong ferroelectric polarization (P_{max}) up to 20 μC/cm at 50 kV/cm. High entropy of A site as ions can effectively disrupt the symmetry of crystal structures, providing additional opportunities to design and tailor the functional properties of entropy-stabilized ferroelectrics.

Zhang et al. [237] used the high-entropy design concept to prepare ferroelectric ceramics $(Ca_{0.2}Sr_{0.2}Ba_{0.2}Pb_{0.2}Nd_{0.1}Na_{0.1})Bi_4Ti_4O_{15}$ (6ABTO). When characterizing the material with an I-V curve, four current peaks are observed. This is the first time such behavior has been reported for an Aurivilius structural ferroelectric material.

As a subset of dielectric materials, high-entropy ferroelectric materials can be widely used in energy storage and conversion, random access memory, and other fields [51,52,81,125,235–247]. Research into this class of materials is growing rapidly, and the future holds great promise. Table 9 summarizes high-entropy ferroelectrics.

TABLE 8

Summary of piezoelectric property of HEOCs.

Materials	Properties	Ref
$Pb(Ni_{0.177}Sc_{0.015}In_{0.06}Ti_{0.32}Nb_{0.428})O_3$	$d_{33} \sim 1210$ pC/N	[230]
$(Bi_{(1-x-y)}Na_{(0.925-x-y)}Li_{0.075})_{0.5}Ba_xSr_yTiO_3$	d_{33} = 133–193 pCN^{-1}	[100]
$Pb(Zr_{0.49}Ti_{0.51})_{0.94}Mn_{0.014}Sb_{0.02}W_{0.014}Ni_{0.02}O_3$	d_{33} = 278 pCN^{-1}	[233]
$Pb_{0.94}Sr_{0.06}(Zr_{0.50}Ti_{0.50})_{0.99}Cr_{0.01}O_3$	d_{33} = 68 pCN^{-1}	[234]
$Pb(Mg_{0.2}Zn_{0.2}Nb_{0.2}Ta_{0.2}W_{0.2})O_3$–$PbTiO_3$	d_{33} = 92.4 pCN^{-1}	[235]

TABLE 9

Summary of ferroelectric property of HEOCs.

Materials	Key Findings	Ref.
$(NaBiBa)_x(SrCa)_{(1-3x)/2}TiO_3$ (x = 0.18–0.22)	$P_{max} \sim 16.59\mu C/cm^2$, $P_r \sim 1.44\mu C/cm^2$	[244]
$Bi_{0.2}Na_{0.2}Ba_{0.2}Sr_{0.2}Pb_{0.2}TiO_3$	$P_{max} \sim 24.2\mu C/cm^2$, $P_r \sim 20.5\mu C/cm^2$	[51]
$Bi_{0.2}Li_{0.2}Ba_{0.2}Sr_{0.2}Pb_{0.2}TiO_3$; $Bi_{0.2}Ag_{0.2}Ba_{0.2}Sr_{0.2}Pb_{0.2}TiO_3$; $Bi_{0.2}K_{0.2}Ba_{0.2}Sr_{0.2}Pb_{0.2}TiO_3$	$P_{max} \sim$ 16-22μC/cm^2, $P_r \sim$ 13-17μC/cm^2	[51]
$(1-x)Pb(Mg_{0.2}Zn_{0.2}Nb_{0.2}Ta_{0.2}W_{0.2})O_3$–$xPbTiO_3$	$P_{max} \sim$ 19-25μC/cm^2, $P_r \sim$ 3-16μC/cm^2	[235]

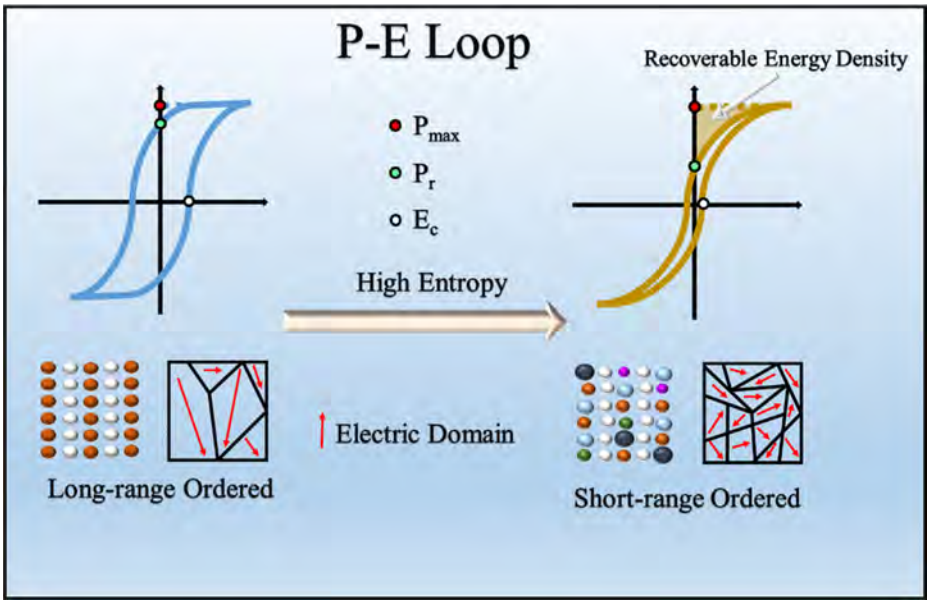

FIG. 14

The change of P-E loop by entropy engineering (the shaded area represents the recoverable energy density, W_{rec}).

TABLE 10

Summary of energy storage property of HEOCs.

Materials	Key Findings	Ref.
$(Na_{0.2}Bi_{0.2}Ba_{0.2}Sr_{0.2}Ca_{0.2})TiO_3$	W_{rec} = 1.02 J/cm^3	[250]
Li_2CO_3-densified $Bi_{0.2}Na_{0.2}Ba_{0.2}Sr_{0.2}Ca_{0.2}TiO_3$	W_{rec} = 10.7 J/cm^3, η = 89 %	[177]
$(Bi_{0.2}Na_{0.2}Ba_{0.2}Sr_{0.2}Ca_{0.2})TiO_3$-xmol%PbO	W_{rec} = 8.2 J/cm^3, η = 92.2 %	[251]
$(Na_{0.2}Bi_{0.2}Ca_{0.2}Sr_{0.2}Ba_{0.2})TiO_3$-0.5 wt%$MnCO_3$	W_{rec} = 1.56 J/cm^3, η = 70.2 %	[252]
$0.91(0.9Ba(Ti_{0.97}Ca_{0.03})O_3$-$0.1Bi_{0.55}Na_{0.45}TiO_3)$-$0.09Bi(Li_{0.2}Y_{0.2}Mg_{0.2}Ti_{0.2}Ta_{0.2})O_3$	W_{rec} = 4.89 J/cm^3, η = 91.2 %	[253]

Energy storage property

Energy storage in high entropy dielectrics represents a cutting-edge field of study with tremendous potential [248]. High entropy dielectrics, characterized by their complex crystal structures and equimolar ratios of multiple cations, offer exceptional properties that make them highly desirable for energy storage applications [177]. In equimolar proportions, the crystal lattice evenly distributes different elements, causing a transformation of the initially long-range ordered electric dipole into a state of short-range order. Consequently, the P-E test reveals a narrower hysteresis loop as an outcome [249]. The combination of high entropy and relaxor behavior in these materials leads to reduced residual polarization (P_r), and coercive field (E_c), resulting in improved recoverable energy storage density (W_{rec}) and efficiency (η) (Fig. 14).

This unique feature allows for increased W_{rec}, η, and power density (P_D) for energy storage devices. Researchers are actively exploring the underlying mechanisms and optimizing the performance of high entropy relaxor ferroelectrics to unlock their full potential and revolutionize energy storage technologies (Table 10).

Chen et al. [249] conducted a high-entropy conversion process on $(K_{0.2}Na_{0.8})NbO_3$ (KNN), leading to the successful synthesis of a single-phase high entropy ceramic known as $[(K_{0.2}Na_{0.8})_{0.8}Li_{0.08}Ba_{0.02}Bi_{0.1}](Nb_{0.68}Sc_{0.02}Hf_{0.08}Zr_{0.1}Ta_{0.08}Sb_{0.04})O_3$ (KNN-H). Through the implementation of the high-entropy approach, numerous localized polymorphic deformations occur within the ceramic material. These distortions within the material create nanoscale electric domains, which contribute to a delay in saturation polarization and a significant enhancement of the breakdown field strength (E_b). Remarkably, the high-entropy KNN-H ceramic exhibits an exceptionally high W_{rec} of 10.06 J/cm^3, along with an impressive η of 90.8 %.

Conclusion

The emergence of HEOCs carries profound innovative significance. These ceramics harness the combined potential of multiple elements to create unique properties through the entropic stabilizing effects they offer. This article initiates by introducing the fundamental concept of entropy. It then demonstrates the rationale behind introducing HEOCs to achieve entropy-stabilizing effects using illustrative examples. A detailed examination of the microstructure of HEOCs uncovers a uniform distribution of cations and lattice adjustments among anions. Additionally, it conducts a thorough analysis of electronic structures through the aid of DFT theoretical calculations. Structural

prediction of HEOCs can be accomplished through various methods, including DFT, MD, CALPHAD, and machine learning. Notably, DFT can employ auxiliary tools like SQS supercells to mitigate computational complexities.

HEOCs predominantly exhibit crystal structures such as rock salt, fluorite, perovskite, spinel, and pyrochlore. These structural variations lead to differences in performance among HEOCs. Diverse preparation processes play a pivotal role in determining the microstructure of the end product, which in turn impacts its overall performance. The selection of an appropriate strategy can yield HEOCs with outstanding properties. Finally, the article provides a comprehensive summary of the various properties and applications of HEOCs. With their incorporation of multiple elements, HEOCs exhibit significant developmental potential in the realms of thermal conductivity, catalysis, ion conduction, magnetism, and electrical properties.

Opportunities and challenges

New HEOC systems possess the potential to exploit artificial intelligence (AI) and other theoretical calculations for material design. By incorporating AI techniques, researchers can explore an extensive design space and accurately predict the properties of HEOCs. As the field of HEOCs continues to progress, the availability of comprehensive experimental data will further enhance the precision of theoretical predictions. First, AI predictions can aid in determining the constituent elements of high-entropy oxide ceramics, thus avoiding laborious experimental procedures. Second, AI can assist in predicting the microstructure and potential properties of HEOCs. With the utilization of cutting-edge technologies, a breakthrough in the correlation between high-entropy systems and individual components is anticipated. Lastly, multi-dimensional predictions can accelerate the development of new HEOCs.

While high-entropy effects have demonstrated significant performance improvements, there still exists some enigma regarding the underlying mechanisms governing these effects. Future research endeavors should prioritize conducting in-depth studies to unravel the intricate mechanisms associated with the entropy effect. Utilizing advanced characterization techniques such as scanning transmission electron microscopy (STEM), neutron diffraction (ND), and atomic force microscopy (AFM) can shed light on the entropy effect of HEOCs. In-situ testing can provide valuable insights into the dynamic impact of entropy effects on the system. Understanding the influence of high entropy on microstructure and properties is paramount to advancing HEOC materials. An essential aspect of high entropy is its capability to effectively modulate long-range order, offering potential applications in developing structures with order–disorder characteristics. Expanding the exploration of HEOCs in this direction has the potential to yield innovative materials with distinct properties and functionality.

HEOCs hold immense potential across various applications, including energy storage, catalysis, electronics, and more. Notably, piezoelectric actuators utilizing the properties of piezoelectric ceramics are vital devices in fields such as ultrasound transmitters and medical imaging. Additionally, a range of resistive devices, including moisture-sensitive, photosensitive, and thermistor devices, can benefit from HEOCs. High-temperature-resistant ceramics play a crucial role in areas like nuclear energy experiments and thermonuclear fusion. Further advancements in HEOC research will pave the way for transformative technologies and materials, enabling the resolution of key challenges in diverse industries.

CRediT authorship contribution statement

Yitao Jiao: Writing – original draft, Investigation. **Jian Dai:** Validation. **Zhenhao Fan:** Formal analysis. **Junye Cheng:** Software. **Guangping Zheng:** Writing – review & editing. **Lawan Grema:** Visualization. **Junwen Zhong:** Writing – review & editing. **Hai-Feng Li:** Writing – review & editing, Supervision, Funding acquisition. **Dawei Wang:** Writing – review & editing, Supervision, Resources, Funding acquisition.

Data availability

Data will be made available on request.

Declaration of competing interest

The authors declare that they have no known competing financial interests or personal relationships that could have appeared to influence the work reported in this paper.

Acknowledgements

This research is supported by the Science and Technology Development Fund, Macao SAR (File Nos. 0051/2019/AFJ and 0090/2021/A2), and Hong Kong, Macao and Taiwan exchange program of HIT.

References

[1] J.-W. Yeh et al., Adv. Eng. Mater. 6 (5) (2004) 299–303. https://doi.org/10.1002/adem.200300567.
[2] A. Sarkar et al., Adv Mater 31 (26) (2019). https://doi.org/10.1002/ADMA.201806236.
[3] M. H. Tsai, et al., 2 (3) (2014) 107–123, doi: https://doi.org/10.1080/21663831.2014.912690.
[4] T.K. Chen et al., Surf. Coat. Technol. 200 (5–6) (2005) 1361–1365. https://doi.org/10.1016/J.SURFCOAT.2005.08.081.
[5] C.H. Lai et al., Surf. Coat. Technol. 201 (6) (2006) 3275–3280. https://doi.org/10.1016/J.SURFCOAT.2006.06.048.
[6] C.M. Rost et al., Nat. Commun. 6 (1) (2015) 8485. https://doi.org/10.1038/ncomms9485.
[7] C. Oses et al., Nat. Rev. Mater. 5 (4) (2020) 295–309. https://doi.org/10.1038/S41578-019-0170-8.
[8] S. Akrami et al., Mater. Sci. Eng. R. Rep. 146 (2021) 100644. https://doi.org/10.1016/J.MSER.2021.100644.
[9] J.M. Schneider, J. Appl. Phys. 130 (15) (2021) 150903. https://doi.org/10.1063/5.0062523.
[10] Z. Zhao et al., J. Mater. Sci. Technol. 35 (11) (2019) 2647–2651. https://doi.org/10.1016/J.JMST.2019.05.054.
[11] X. Yan et al., J. Am. Ceram. Soc. 101 (10) (2018) 4486–4491. https://doi.org/10.1111/JACE.15779.
[12] Y. Qin et al., J. Adv. Ceram. 8 (1) (2019) 148–152. https://doi.org/10.1007/S40145-019-0319-3/METRICS.
[13] H. Chen et al., J. Mater. Sci. Technol. 35 (8) (2019) 1700. https://doi.org/10.1016/J.JMST.2019.04.006.
[14] H. Chen et al., J. Mater. Sci. Technol. 35 (10) (2019) 2404–2408. https://doi.org/10.1016/J.JMST.2019.05.059.
[15] B. Ye et al., Acta Mater. 170 (2019) 15–23. https://doi.org/10.1016/J.ACTAMAT.2019.03.021.
[16] T.J. Harrington et al., Acta Mater. 166 (2019) 271–280. https://doi.org/10.1016/J.ACTAMAT.2018.12.054.
[17] X. Ren et al., Scr. Mater. 168 (2019) 47–50. https://doi.org/10.1016/J.SCRIPTAMAT.2019.04.018.

[18] R. Liu et al., Adv. Mater. 29 (38) (2017) 1702712. https://doi.org/10.1002/ADMA.201702712.
[19] C.M. Rost et al., J. Am. Ceram. Soc. 100 (6) (2017) 2732–2738. https://doi.org/10.1111/JACE.14756.
[20] F.Z. Dai et al., J. Mater. Sci. Technol. 43 (2020) 168–174. https://doi.org/10.1016/J.JMST.2020.01.005.
[21] H. Xiang et al., J. Adv. Ceram. 10 (3) (2021) 385–441. https://doi.org/10.1007/S40145-021-0477-Y.
[22] Z. Rák et al., Mater. Lett. 217 (2018) 300–303. https://doi.org/10.1016/J.MATLET.2018.01.111.
[23] Z. Rak et al., J. Appl. Phys. 120 (9) (2016) 95105. https://doi.org/10.1063/1.4962135.
[24] S.H. Wei et al., Phys. Rev. B 42 (15) (1990) 9622. https://doi.org/10.1103/PhysRevB.42.9622.
[25] A. Zunger et al., Phys. Rev. Lett. 65 (3) (1990) 353. https://doi.org/10.1103/PhysRevLett.65.353.
[26] Y. Liu et al., J. Eur. Ceram. Soc. 40 (15) (2020) 6272–6277. https://doi.org/10.1016/J.JEURCERAMSOC.2020.07.054.
[27] M.C. Gao et al., High-Entropy Alloys: Fundamentals and Applications (2016) 1–516. https://doi.org/10.1007/978-3-319-27013-5/COVER.
[28] B. Ye et al., J. Am. Ceram. Soc. 102 (7) (2019) 4344–4352. https://doi.org/10.1111/JACE.16295.
[29] S. Jiang et al., Ceram. Int. 46 (10) (2020) 15104–15112. https://doi.org/10.1016/J.CERAMINT.2020.03.045.
[30] K.C. Pitike et al., Chem. Mater. 32 (17) (2020) 7507–7515. https://doi.org/10.1021/ACS.CHEMMATER.0C02702/ASSET/IMAGES/LARGE/CM0C02702_0006.JPEG.
[31] G. Anand et al., Acta Mater. 146 (2018) 119–125. https://doi.org/10.1016/J.ACTAMAT.2017.12.037.
[32] K. Kaufmann, et al., npj Comp. Mater. 2020 6:1, 6(1) (2020) 1–9. doi: https://doi.org/10.1038/s41524-020-0317-6.
[33] Y. Zhang et al., Prog. Mater Sci. 61 (2014) 1–93. https://doi.org/10.1016/J.PMATSCI.2013.10.001.
[34] L. Su et al., Adv. Mater. 35 (19) (2023) 2205751. https://doi.org/10.1002/ADMA.202205751.
[35] A. Mao et al., J. Magn. Magn. Mater. 484 (2019) 245–252. https://doi.org/10.1016/j.jmmm.2019.04.023.
[36] D. Bérardan et al., J. Mater. Chem. A 4 (24) (2016) 9536–9541. https://doi.org/10.1039/C6TA03249D.
[37] A. Sarkar et al., Nat. Commun. 9 (1) (2018) 3400. https://doi.org/10.1038/s41467-018-05774-5.
[38] Q. Wang et al., Electrochem. Commun. 100 (2019) 121–125. https://doi.org/10.1016/j.elecom.2019.02.001.
[39] A.J. Wright et al., J. Mater. Sci. 55 (23) (2020) 9812–9827. https://doi.org/10.1007/S10853-020-04583-W.
[40] H. Chen et al., J. Mater. Chem. A 6 (24) (2018) 11129–11133. https://doi.org/10.1039/C8TA01772G.
[41] L. Xu et al., J. Eur. Ceram. Soc. 43 (8) (2023) 3507–3515. https://doi.org/10.1016/J.JEURCERAMSOC.2023.02.003.
[42] J. Gild et al., J. Eur. Ceram. Soc. 38 (10) (2018) 3578–3584. https://doi.org/10.1016/J.JEURCERAMSOC.2018.04.010.
[43] A. Sarkar et al., Dalton Trans. 46 (36) (2017) 12167–12176. https://doi.org/10.1039/C7DT02077E.
[44] K. Chen et al., J. Eur. Ceram. Soc. 38 (11) (2018) 4161–4164. https://doi.org/10.1016/J.JEURCERAMSOC.2018.04.063.
[45] J. Dąbrowa et al., J. Eur. Ceram. Soc. 40 (15) (2020) 5870–5881. https://doi.org/10.1016/J.JEURCERAMSOC.2020.07.014.
[46] X. Chen et al., J. Am. Ceram. Soc. 103 (2) (2020) 750–756. https://doi.org/10.1111/JACE.16842.
[47] Z. Zhao et al., J. Adv. Ceram. 9 (3) (2020) 303–311. https://doi.org/10.1007/S40145-020-0368-7/METRICS.
[48] F. Zhang et al., J. Mater. Sci. Technol. 105 (2022) 122–130. https://doi.org/10.1016/J.JMST.2021.07.028.
[49] L. Chen et al., J. Adv. Ceram. 11 (4) (2022) 556–569. https://doi.org/10.1007/S40145-021-0556-0.
[50] P. Zhang et al., J. Mater. Sci. Technol. 97 (2022) 182–189. https://doi.org/10.1016/j.jmst.2021.05.016.
[51] Z. Liu et al., Ceram. Int. 47 (23) (2021) 33039–33046. https://doi.org/10.1016/J.CERAMINT.2021.08.204.
[52] Y. Liu et al., Ceram. Int. 49 (13) (2023) 21546–21554. https://doi.org/10.1016/J.CERAMINT.2023.03.290.
[53] C. Zhao et al., Angew. Chem. Int. Ed. 59 (1) (2020) 264–269. https://doi.org/10.1002/ANIE.201912171.
[54] A. Kumar et al., J. Materiomics 9 (1) (2023) 191–196. https://doi.org/10.1016/J.JMAT.2022.08.001.
[55] H. Minouei et al., Appl. Surf. Sci. 576 (2022) 151719. https://doi.org/10.1016/J.APSUSC.2021.151719.
[56] H.X. Guo et al., ACS Appl. Mater. Interfaces 14 (1) (2022) 1950–1960. https://doi.org/10.1021/ACSAMI.1C20055/ASSET/IMAGES/LARGE/AM1C20055_0007.JPEG.
[57] H. Minouei et al., J. Power Sources 549 (2022) 232041. https://doi.org/10.1016/J.JPOWSOUR.2022.232041.
[58] F. Jin et al., Ceram. Int. 49 (11) (2023) 16625–16629. https://doi.org/10.1016/J.CERAMINT.2023.02.020.
[59] Z. Lin et al., Ceram. Int. 49 (14) (2023) 23057–23067. https://doi.org/10.1016/J.CERAMINT.2023.04.131.
[60] B. Jiang et al., J. Am. Chem. Soc. 143 (11) (2021) 4193–4204. https://doi.org/10.1021/JACS.0C10739/ASSET/IMAGES/LARGE/JA0C10739_0008.JPEG.
[61] F. Li et al., J. Adv. Ceram. 8 (4) (2019) 576–582. https://doi.org/10.1007/S40145-019-0342-4/METRICS.
[62] A.J. Wright et al., Acta Mater. 211 (2021) 116858. https://doi.org/10.1016/J.ACTAMAT.2021.116858.
[63] A.J. Wright et al., Scr. Mater. 181 (2020) 76–81. https://doi.org/10.1016/J.SCRIPTAMAT.2020.02.011.
[64] H. Xiang et al., J. Mater. Sci. Technol. 93 (2021) 28–32. https://doi.org/10.1016/j.jmst.2021.03.057.
[65] K. Liu et al., Ceram. Int. 48 (16) (2022) 23307–23313. https://doi.org/10.1016/J.CERAMINT.2022.04.317.
[66] D. Bérardan et al., Physica Status Solidi - Rapid Research Letters 10 (4) (2016) 328–333. https://doi.org/10.1002/PSSR.201600043.
[67] D. Berardan et al., J. Alloy. Compd. 704 (2017) 693–700. https://doi.org/10.1016/J.JALLCOM.2017.02.070.
[68] B. Cheng et al., Commun. Chem. 2019 2:1 2 (1) (2019) 1–9. https://doi.org/10.1038/s42004-019-0216-2.
[69] H. Junjie et al., J. Eur. Ceram. Soc. 41 (12) (2021) 6080–6086. https://doi.org/10.1016/J.JEURCERAMSOC.2021.05.044.
[70] Y. Wen et al., Ceram. Int. 48 (2) (2022) 2546–2554. https://doi.org/10.1016/J.CERAMINT.2021.10.037.
[71] Z. Zhao et al., J. Mater. Sci. Technol. 39 (2020) 167–172. https://doi.org/10.1016/J.JMST.2019.08.018.
[72] W. Sang et al., Ceram. Int. (2023) . https://doi.org/10.1016/J.CERAMINT.2023.06.151.
[73] Y. Sharma et al., Phys Rev Mater 2 (6) (2018) . https://doi.org/10.1103/PHYSREVMATERIALS.2.060404.
[74] S. Jiang et al., Scr. Mater. 142 (2018) 116–120. https://doi.org/10.1016/J.SCRIPTAMAT.2017.08.040.
[75] V.M. Goldschmidt, Naturwissenschaften 14 (21) (1926) 477–485. https://doi.org/10.1007/BF01507527.
[76] N. Ramadass, Mater. Sci. Eng. 36 (2) (1978) 231–239. https://doi.org/10.1016/0025-5416(78)90076-9.
[77] Z.J. Corey et al., Adv. Sci. 9 (29) (2022) 2202671. https://doi.org/10.1002/ADVS.202202671.
[78] R. Witte et al., J. Appl. Phys. 127 (18) (2020) . https://doi.org/10.1063/5.0004125.
[79] Y. Ning et al., Ceram. Int. 49 (8) (2023) 12214–12223. https://doi.org/10.1016/J.CERAMINT.2022.12.073.
[80] Y. Yin et al., Appl. Phys. Lett. 120 (8) (2022) 82404. https://doi.org/10.1063/5.0081688/2833152.
[81] S. Zhou et al., Ceram. Int. 46 (6) (2020) 7430–7437. https://doi.org/10.1016/J.CERAMINT.2019.11.239.
[82] P. Edalati et al., J Mater Chem A Mater 8 (7) (2020) 3814–3821. https://doi.org/10.1039/C9TA12846H.
[83] T. Maiti et al., ACS Sustain. Chem. Eng. 8 (46) (2020) 17022–17032. https://doi.org/10.1021/ACSSUSCHEMENG.0C03849/ASSET/IMAGES/LARGE/SC0C03849_0008.JPEG.
[84] S. Zhou et al., Chem. Eng. J. 427 (2022) 131684. https://doi.org/10.1016/J.CEJ.2021.131684.
[85] J. Dąbrowa et al., Mater. Lett. 216 (2018) 32–36. https://doi.org/10.1016/J.MATLET.2017.12.148.
[86] M. Stygar et al., J. Eur. Ceram. Soc. 40 (4) (2020) 1644–1650. https://doi.org/10.1016/J.JEURCERAMSOC.2019.11.030.
[87] W. Bian et al., Electrochim. Acta 447 (2023) 142157. https://doi.org/10.1016/J.ELECTACTA.2023.142157.
[88] A.R. West, Solid state chemistry and its applications, John Wiley & Sons, 2022.
[89] H.R. Mao et al., J. Eur. Ceram. Soc. 41 (4) (2021) 2855–2860. https://doi.org/10.1016/J.JEURCERAMSOC.2020.11.052.

[90] D.A. Vinnik et al., Ceram. Int. 45 (10) (2019) 12942–12948. https://doi.org/10.1016/J.CERAMINT.2019.03.221.
[91] K.P. Tseng et al., J. Am. Ceram. Soc. 103 (1) (2020) 569–576. https://doi.org/10.1111/JACE.16689.
[92] Z. Zhao et al., J. Mater. Sci. Technol. 35 (10) (2019) 2227–2231. https://doi.org/10.1016/J.JMST.2019.05.030.
[93] Z. Grzesik et al., J. Eur. Ceram. Soc. 40 (3) (2020) 835–839. https://doi.org/10.1016/J.JEURCERAMSOC.2019.10.026.
[94] Z. Teng et al., J. Eur. Ceram. Soc. 40 (4) (2020) 1639–1643. https://doi.org/10.1016/J.JEURCERAMSOC.2019.12.008.
[95] J. Chen et al., J. Phys. Chem. C 123 (29) (2019) 17735–17744. https://doi.org/10.1021/ACS.JPCC.9B04992.
[96] A.D. Dupuy et al., Mater Res Lett 7 (2) (2019) 60–67. https://doi.org/10.1080/21663831.2018.1554605.
[97] H. Chen et al., J. Mater. Sci. Technol. 36 (2020) 134–139. https://doi.org/10.1016/J.JMST.2019.07.022.
[98] D.A. Vinnik et al., Ceram. Int. 46 (7) (2020) 9656–9660. https://doi.org/10.1016/J.CERAMINT.2019.12.232.
[99] H. Chen et al., RSC Adv. 10 (16) (2020) 9736–9744. https://doi.org/10.1039/D0RA00255K.
[100] D. Lin et al., Curr. Appl Phys. 9 (6) (2009) 1369–1374. https://doi.org/10.1016/J.CAP.2009.03.001.
[101] D. Wang et al., J. Adv. Dielectr. 8 (5) (2018) 1830004. https://doi.org/10.1142/S2010135X18300049.
[102] I. Bekri-Abbes et al., J. Polym. Res. 18 (4) (2011) 659–665. https://doi.org/10.1007/S10965-010-9461-X/TABLES/2.
[103] Y. Ben Smida et al., Synthesis Methods and Crystallization (2020) . https://doi.org/10.5772/INTECHOPEN.93337.
[104] S. Kumari et al., J. Mater. Sci. Mater. Electron. 32 (12) (2021) 16900–16915. https://doi.org/10.1007/S10854-021-06252-3/TABLES/5.
[105] K. Wang et al., Ceram. Int. 46 (11) (2020) 18358–18361. https://doi.org/10.1016/J.CERAMINT.2020.04.060.
[106] J. Liu et al., Ceram. Int. 46 (12) (2020) 20576–20581. https://doi.org/10.1016/J.CERAMINT.2020.05.090.
[107] B. Ma et al., J. Am. Ceram. Soc. 105 (6) (2022) 3765–3773. https://doi.org/10.1111/JACE.18343.
[108] C.E.J. Dancer, Mater. Res. Express 3 (10) (2016) 102001. https://doi.org/10.1088/2053-1591/3/10/102001.
[109] B. Yoon et al., Adv. Eng. Mater. 25 (5) (2023) 2200731. https://doi.org/10.1002/ADEM.202200731.
[110] O. Guillon et al., Adv. Eng. Mater. 16 (7) (2014) 830–849. https://doi.org/10.1002/ADEM.201300409.
[111] S.K. Sun et al., J. Am. Ceram. Soc. (2023) . https://doi.org/10.1111/JACE.19499.
[112] M. Qin et al., J. Eur. Ceram. Soc. 40 (12) (2020) 4348–4353. https://doi.org/10.1016/j.jeurceramsoc.2020.03.063.
[113] I. Shishkovsky, Sintering of Functional Materials, BoD–Books on Demand, 2018.
[114] M. Suárez et al., Sintering applications, InTech, Croatia, 2013.
[115] M. Biesuz et al., Journal of Asian Ceramic Societies 7 (2) (2019) 127–132. https://doi.org/10.1080/21870764.2019.1595931.
[116] S.G. Savio et al., Ceram. Int. (2024) . https://doi.org/10.1016/J.CERAMINT.2024.01.078.
[117] Y. Chen et al., Ceram. Int. (2024) . https://doi.org/10.1016/J.CERAMINT.2024.02.174.
[118] I.Y. Buravlev et al., Ceram. Int. (2024) . https://doi.org/10.1016/J.CERAMINT.2024.01.357.
[119] G.B. Nair et al., Energy (2018) 411–431. https://doi.org/10.1016/B978-0-12-813731-4.00013-8.
[120] N.S. Bajaj et al., Energy Mater.: Fundament. Appl. (2021) 61–82. https://doi.org/10.1016/B978-0-12-823710-6.00019-4.
[121] A. Radoń et al., Sci. Rep. 9 (1) (2019) . https://doi.org/10.1038/S41598-019-56586-6.
[122] M.H. Khatun et al., Mater. Res. Express 11 (1) (2024) 016102. https://doi.org/10.1088/2053-1591/AD1D87.
[123] Y. Iriani et al., Integr. Ferroelectr. 240 (1) (2024) 140–148. https://doi.org/10.1080/10584587.2023.2296318.
[124] P. Thakur et al., Mater. Res. Express 3 (2016) . https://doi.org/10.1088/2053-1591/3/7/075001.
[125] Y.W. Chen et al., Ceram. Int. 47 (8) (2021) 11451–11458. https://doi.org/10.1016/J.CERAMINT.2020.12.272.
[126] A. Sarkar et al., J. Eur. Ceram. Soc. 37 (2) (2017) 747–754. https://doi.org/10.1016/J.JEURCERAMSOC.2016.09.018.
[127] J. Li, Q. Wu, and J. Wu, "Handbook of nanoparticles," 2015.
[128] Q. Jiang et al., Chem. Eng. J. 453 (2023) 139510. https://doi.org/10.1016/J.CEJ.2022.139510.
[129] T.X. Nguyen et al., Adv. Funct. Mater. (2023) 2300509. https://doi.org/10.1002/ADFM.202300509.
[130] D. Wang et al., J. Colloid Interface Sci. 646 (2023) 89–97. https://doi.org/10.1016/J.JCIS.2023.05.043.
[131] Y. Wang et al., J. Mater. Res. Technol. 29 (2024) 1131–1154. https://doi.org/10.1016/J.JMRT.2024.01.186.
[132] A. Saremi et al., Solid State Sci. 148 (2024) 107432. https://doi.org/10.1016/J.SOLIDSTATESCIENCES.2023.107432.
[133] Y. Bian et al., Processes 6 (8) (2018) 122. https://doi.org/10.3390/PR6080122.
[134] A. Mao et al., J. Magn. Magn. Mater. 484 (2019) 245–252. https://doi.org/10.1016/J.JMMM.2019.04.023.
[135] F.T. Li et al., Nanoscale 7 (42) (2015) 17590–17610. https://doi.org/10.1039/C5NR05299H.
[136] C. Zuo et al., Ceram. Int. 49 (15) (2023) 25486–25494. https://doi.org/10.1016/J.CERAMINT.2023.05.089.
[137] Y. Chu et al., Sci. China Mater. 65 (11) (2022) 3144–3149. https://doi.org/10.1007/S40843-022-2080-5/METRICS.
[138] K. Zhang et al., J. Alloy. Compd. 817 (2020) 153328. https://doi.org/10.1016/J.JALLCOM.2019.153328.
[139] S. Aydinyan et al., Ceram. Int. 48 (14) (2022) 20294–20305. https://doi.org/10.1016/J.CERAMINT.2022.03.310.
[140] N.R. De Tacconi et al., ChemPhysChem 13 (12) (2012) 2945–2955. https://doi.org/10.1002/CPHC.201200046.
[141] M. Lackner, Combustion synthesis: novel routes to novel materials, Bentham Science Publishers, 2010.
[142] F.T. Li et al., Cat. Sci. Technol. 2 (7) (2012) 1455–1462. https://doi.org/10.1039/C2CY00485B.
[143] M.V. Chudakova et al., Chem. Eng. Sci. 284 (2024) 119408. https://doi.org/10.1016/J.CES.2023.119408.
[144] C. Özyalcin et al., Appl. Energy 353 (2024) 122045. https://doi.org/10.1016/J.APENERGY.2023.122045.
[145] A. Khort et al., Scientific Reports 11 (1) (2021) 1–14. https://doi.org/10.1038/s41598-021-87250-7.
[146] J. Sushil et al., Mater. Chem. Phys. 259 (2021) . https://doi.org/10.1016/J.MATCHEMPHYS.2020.124014.
[147] M.S. Lal et al., ACS Appl. Mater. Interfaces 11 (34) (2019) 30846–30857. https://doi.org/10.1021/ACSAMI.9B08794.
[148] T. Parida et al., Scr. Mater. 178 (2020) 513–517. https://doi.org/10.1016/J.SCRIPTAMAT.2019.12.027.
[149] C. Kumar, J. Mater. Sci. Mater. Electron. 22 (6) (2011) 579–582. https://doi.org/10.1007/S10854-010-0179-7/FIGURES/6.
[150] L. Shen et al., Appl Catal B 295 (2021) 120264. https://doi.org/10.1016/J.APCATB.2021.120264.
[151] P. Ma et al., RSC Adv. 6 (39) (2016) 32947–32955. https://doi.org/10.1039/C6RA03300H.
[152] M.R. Chellali et al., Scr. Mater. 166 (2019) 58–63. https://doi.org/10.1016/J.SCRIPTAMAT.2019.02.039.
[153] J. Wang et al., Sci. Reports 10 (1) (2020) 1–13. https://doi.org/10.1038/s41598-020-75134-1.
[154] D.S. Jung et al., Korean J. Chem. Eng. 27 (6) (2010) 1621–1645. https://doi.org/10.1007/S11814-010-0402-5.
[155] B. Thiébaut, Platin. Met. Rev. 55 (2) (2011) 149–151. https://doi.org/10.1595/147106711X567680.
[156] R. Strobel et al., Adv. Powder Technol. 17 (5) (2006) 457–480. https://doi.org/10.1163/156855206778440525.
[157] R. Strobel et al., Platin. Met. Rev. 53 (1) (2009) 11–20. https://doi.org/10.1595/147106709X392993.
[158] M.B. Kumar et al., Process. Appl. Ceram. 6 (3) (2012) 165–171. https://doi.org/10.2298/PAC1203165K.
[159] A.J. Gröhn et al., Ind. Eng. Chem. Res. 53 (26) (2014) 10734–10742. https://doi.org/10.1021/IE501709S.
[160] S. Shin et al., Adv Eng Mater (2024) 2301515. https://doi.org/10.1002/ADEM.202301515.
[161] T. Ravikumar et al., Colloids Surf A Physicochem Eng Asp 686 (2024) 133382. https://doi.org/10.1016/J.COLSURFA.2024.133382.
[162] I. Safi, Surf. Coat. Technol. 127 (2–3) (2000) 203–218. https://doi.org/10.1016/S0257-8972(00)00566-1.
[163] W.D. Sproul et al., Thin Solid Films 491 (1–2) (2005) 1–17. https://doi.org/10.1016/J.TSF.2005.05.022.
[164] S. Berg et al., Thin Solid Films 476 (2) (2005) 215–230. https://doi.org/10.1016/J.TSF.2004.10.051.

[165] A. Kirnbauer et al., Vacuum 168 (2019) 108850. https://doi.org/10.1016/J.VACUUM.2019.108850.
[166] S. Yamada et al., Appl. Phys Express (2024) . https://doi.org/10.35848/1882-0786/AD2783.
[167] J.G. Anjana et al., Mater. Res. Express 11 (1) (2024) 016403. https://doi.org/10.1088/2053-1591/AD1E0F.
[168] A. Iqbal et al., Sensors 18 (6) (2018) 1797. https://doi.org/10.3390/S18061797.
[169] Z.Y. Tan et al., Mater. Lett. 330 (2023) 133381. https://doi.org/10.1016/J.MATLET.2022.133381.
[170] M. Biesuz et al., J. Mater. Sci. 53 (11) (2018) 8074–8085. https://doi.org/10.1007/S10853-018-2168-9/FIGURES/10.
[171] L. Spiridigliozzi et al., Materials 13 (3) (2020) 558. https://doi.org/10.3390/MA13030558.
[172] A. Salian et al., ACS Appl Electron Mater (2023) . https://doi.org/10.1021/ACSAELM.3C00094/ASSET/IMAGES/LARGE/EL3C00094_0013.JPEG.
[173] Y. Xu et al., Sep. Purif. Technol. 290 (2022) 120844. https://doi.org/10.1016/J.SEPPUR.2022.120844.
[174] D. Stenzel et al., Front. Energy Res. 10 (2022) 942314. https://doi.org/10.3389/fenrg.2022.942314.
[175] L. Eiselt et al., Int. J. Appl. Ceram. Technol. 20 (1) (2023) 213–223. https://doi.org/10.1111/IJAC.14150.
[176] A.H. Phakatkar et al., Langmuir 37 (30) (2021) 9059–9068. https://doi.org/10.1021/ACS.LANGMUIR.1C01105/ASSET/IMAGES/LARGE/LA1C01105_0006.JPEG.
[177] J. Guo et al., Nano Energy 112 (2023) 108458. https://doi.org/10.1016/J.NANOEN.2023.108458.
[178] P. Ghigna et al., ACS Appl. Mater. Interfaces 12 (45) (2020) 50344–50354. https://doi.org/10.1021/ACSAMI.0C13161.
[179] H. Chen et al., ACS Mater Lett 1 (1) (2019) 83–88. https://doi.org/10.1021/ACSMATERIALSLETT.9B00064.
[180] A. Mao et al., J. Magn. Magn. Mater. 484 (2019) 245–252. https://doi.org/10.1016/J.JMMM.2019.04.023.
[181] M. Balcerzak et al., J. Electron. Mater. 48 (11) (2019) 7105–7113. https://doi.org/10.1007/S11664-019-07512-Z.
[182] W. Hong et al., J. Am. Ceram. Soc. 102 (4) (2019) 2228–2237. https://doi.org/10.1111/jace.16075.
[183] A.J. Wright et al., J. Eur. Ceram. Soc. 40 (5) (2020) 2120–2129. https://doi.org/10.1016/J.JEURCERAMSOC.2020.01.015.
[184] D.A. Vinnik et al., Nanomaterials 10 (2) (2020) 268. https://doi.org/10.3390/NANO10020268.
[185] R. Witte et al., Phys. Rev. Mater. 3 (3) (2019) 034406. https://doi.org/10.1103/PhysRevMaterials.3.034406.
[186] Z. Zhao et al., J. Mater. Sci. Technol. 47 (2020) 45–51. https://doi.org/10.1016/j.jmst.2020.02.011.
[187] J. Yan et al., J. Mater. Sci. 55 (16) (Jun. 2020) 6942–6951. https://doi.org/10.1007/S10853-020-04482-0.
[188] F. Okejiri et al., ChemSusChem 13 (1) (2020) 111–115. https://doi.org/10.1002/CSSC.201902705.
[189] A. Mao et al., J. Magn. Magn. Mater. 497 (2020) 165884. https://doi.org/10.1016/j.jmmm.2019.165884.
[190] M. Zamani et al., J. Mol. Liq. 274 (2019) 60–67. https://doi.org/10.1016/J.MOLLIQ.2018.10.083.
[191] A. Mao et al., J. Mol. Struct. 1194 (2019) 11–18. https://doi.org/10.1016/J.MOLSTRUC.2019.05.073.
[192] K. Ren et al., Scr. Mater. 178 (2020) 382–386. https://doi.org/10.1016/J.SCRIPTAMAT.2019.12.006.
[193] D. Liu et al., Ceram. Int. 47 (21) (2021) 29960–29968. https://doi.org/10.1016/J.CERAMINT.2021.07.170.
[194] J.L. Braun et al., Adv. Mater. 30 (51) (2018) 1805004. https://doi.org/10.1002/ADMA.201805004.
[195] J. Zhu et al., J. Eur. Ceram. Soc. 41 (1) (2021) 1052–1057. https://doi.org/10.1016/J.JEURCERAMSOC.2020.08.070.
[196] T. Wang et al., J. Am. Chem. Soc. 142 (10) (2020) 4550–4554. https://doi.org/10.1021/JACS.9B12377/ASSET/IMAGES/LARGE/JA9B12377_0004.JPEG.
[197] Y. Zhang et al., ACS Appl. Mater. Interfaces 12 (29) (2020) 32548–32555. https://doi.org/10.1021/ACSAMI.0C05916/ASSET/IMAGES/LARGE/AM0C05916_0005.JPEG.
[198] Y. Zheng et al., Energy Storage Mater. 23 (2019) 678–683. https://doi.org/10.1016/J.ENSM.2019.02.030.
[199] H. Xu et al., Nat. Commun. 11 (1) (2020) 3908. https://doi.org/10.1038/S41467-020-17738-9.
[200] H. Chen et al., Appl Catal B 276 (2020) 119155. https://doi.org/10.1016/J.APCATB.2020.119155.
[201] N. Qiu et al., J. Alloy. Compd. 777 (2019) 767–774. https://doi.org/10.1016/J.JALLCOM.2018.11.049.
[202] N. Osenciat et al., J. Am. Ceram. Soc. 102 (10) (2019) 6156–6162. https://doi.org/10.1111/JACE.16511.
[203] M. Gazda et al., ACS Mater Lett 2 (10) (2020) 1315–1321. https://doi.org/10.1021/ACSMATERIALSLETT.0C00257/ASSET/IMAGES/MEDIUM/TZ0C00257_M002.GIF.
[204] R. Guo et al., ACS Mater Lett 4 (9) (2022) 1646–1652. https://doi.org/10.1021/acsmaterialslett.2c00542.
[205] Q. Yang et al., J. Alloy. Compd. 872 (2021) 159633. https://doi.org/10.1016/J.JALLCOM.2021.159633.
[206] Z. Liu et al., Nanomicro Lett 14 (1) (2022) 1–16. https://doi.org/10.1007/S40820-022-00967-6/FIGURES/5.
[207] Y. Sharma et al., Phys Rev Mater 4 (1) (2020) 014404. https://doi.org/10.1103/PhysRevMaterials.4.014404.
[208] K. Simeonidis et al., EPJ Web of Conferences (2013) . https://doi.org/10.1051/epjconf/20134008007.
[209] A. Sarkar et al., Dalton Trans 50 (6) (2021) 1973–1982. https://doi.org/10.1039/d0dt04154h.
[210] P.B. Meisenheimer et al., Sci. Rep. 7 (1) (2017) 13344. https://doi.org/10.1038/s41598-017-13810-5.
[211] J. Zhang et al., Chem. Mater. 31 (10) (2019) 3705–3711. https://doi.org/10.1021/acs.chemmater.9b00624.
[212] M.P. Jimenez-Segura et al., Appl. Phys. Lett. 114 (12) (2019) 122401. https://doi.org/10.1063/1.5091787.
[213] A. Mao et al., J. Magn. Magn. Mater. 503 (2020) 166594. https://doi.org/10.1016/J.JMMM.2020.166594.
[214] A. Mao et al., J. Magn. Magn. Mater. 497 (2020) 165884. https://doi.org/10.1016/J.JMMM.2019.165884.
[215] K. Edalati et al., Mater Res Lett 3 (4) (2015) 216–221. https://doi.org/10.1080/21663831.2015.1065454.
[216] S. Zhou et al., J. Am. Ceram. Soc. 105 (7) (2022) 4796–4804. https://doi.org/10.1111/JACE.18455.
[217] Z. Lou et al., J. Mater. Res. Technol. 21 (2022) 850–858. https://doi.org/10.1016/J.JMRT.2022.09.081.
[218] H. Liu et al., Ceram. Int. 49 (5) (2023) 7208–7213. https://doi.org/10.1016/J.CERAMINT.2022.04.318.
[219] Z. Zheng et al., Ceram. Int. (2023) 32521–32527. https://doi.org/10.1016/J.CERAMINT.2023.07.215.
[220] Q. Du et al., J. Mater. Sci. Mater. Electron. 31 (10) (2020) 7760–7765. https://doi.org/10.1007/S10854-020-03313-X/FIGURES/9.
[221] H. Qin et al., Microstructures 3 (4) (2023) 2023035. https://doi.org/10.20517/MICROSTRUCTURES.2023.34.
[222] H. Qin, et al., J., Adv. Dielectr. 13 (2023) 2350018. https://doi.org/10.1142/S2010135X23500182.
[223] X. Zhou et al., Prog. Mater Sci. 122 (2021) 100836. https://doi.org/10.1016/J.PMATSCI.2021.100836.
[224] J. Hao et al., Mater. Sci. Eng. R. Rep. 135 (2019) 1–57. https://doi.org/10.1016/J.MSER.2018.08.001.
[225] F. Li et al., Adv. Funct. Mater. 28 (37) (2018) 1801504. https://doi.org/10.1002/ADFM.201801504.
[226] M.H. Zhang et al., Nat. Commun. 13 (1) (2022) 1–10. https://doi.org/10.1038/s41467-022-31158-x.
[227] Y. Huang et al., Nat. Commun. 12 (1) (2021) 1–8. https://doi.org/10.1038/s41467-020-20662-7.
[228] S. Wang et al., J. Am. Ceram. Soc. (2023) 205–213. https://doi.org/10.1111/JACE.19426.
[229] J. Zhao et al., J. Materiomics 10 (2) (2023) 416–422. https://doi.org/10.1016/J.JMAT.2023.07.001.
[230] Y. Liu et al., Acta Mater. 236 (2022) 118115. https://doi.org/10.1016/J.ACTAMAT.2022.118115.
[231] M. Zhang et al., Mater. Des. 200 (2021) 109447. https://doi.org/10.1016/J.MATDES.2020.109447.
[232] S. Zhang, Microstructures 3 (1) (2023) 2023003. https://doi.org/10.20517/MICROSTRUCTURES.2022.38.
[233] D. Bochenek et al., J. Phys. Chem. Solid 133 (2019) 128–134. https://doi.org/10.1016/J.JPCS.2019.05.015.
[234] R. Zachariasz et al., Eur. Phys. J. B 88 (11) (2015) 296. https://doi.org/10.1140/EPJB/E2015-60420-Y.
[235] X. Li et al., Ceram. Int. 48 (9) (2022) 12848–12855. https://doi.org/10.1016/J.CERAMINT.2022.01.156.
[236] N. Setter et al., J. Appl. Phys. 51 (8) (1980) 4356–4360. https://doi.org/10.1063/1.328296.

[237] M. Zhang et al., Acta Mater. 229 (2022) 117815. https://doi.org/10.1016/J.ACTAMAT.2022.117815.
[238] L. Shao et al., J. Alloy. Compd. 954 (2023) 170205. https://doi.org/10.1016/J.JALLCOM.2023.170205.
[239] W. Ye et al., J. Am. Ceram. Soc. (2023) 6858–6867. https://doi.org/10.1111/JACE.19329.
[240] G.N. Kotsonis et al., J. Am. Ceram. Soc. 106 (10) (2023) 5587–5611. https://doi.org/10.1111/JACE.19252.
[241] D. Damjanovic, Rep. Prog. Phys. 61 (9) (1998) 1267. https://doi.org/10.1088/0034-4885/61/9/002.
[242] J. Liu et al., J. Mater. Sci. Technol. 130 (2022) 103–111. https://doi.org/10.1016/J.JMST.2022.05.012.
[243] Z. Hu et al., J. Eur. Ceram. Soc. 43 (1) (2023) 177–182. https://doi.org/10.1016/J.JEURCERAMSOC.2022.09.045.
[244] Y. Shang et al., J. Mater. Sci. Mater. Electron. 33 (8) (2022) 5359–5369. https://doi.org/10.1007/S10854-022-07731-X/FIGURES/10.
[245] Y. Liu et al., Prog. Mater Sci. 127 (2022) 100943. https://doi.org/10.1016/J.PMATSCI.2022.100943.
[246] N. Setter et al., J. Appl. Phys. 100 (5) (2006) 051606. https://doi.org/10.1063/1.2336999/974388.
[247] I.J. Kim et al., Adv. Mater. 35 (22) (2023) 2206864. https://doi.org/10.1002/ADMA.202206864.
[248] Z. Lu et al., J. Adv. Dielectr. 13 (2022) 2242006. https://doi.org/10.1142/S2010135X22420061.
[249] L. Chen et al., Nat. Commun. 13 (1) (2022) 1–8. https://doi.org/10.1038/s41467-022-30821-7.
[250] Y. Pu et al., Appl. Phys. Lett. 115 (22) (2019) 223901. https://doi.org/10.1063/1.5126652/37351.
[251] J. Guo et al., Adv. Electron. Mater. 8 (11) (2022) 2200503. https://doi.org/10.1002/AELM.202200503.
[252] J. Fang et al., Results Phys. 38 (2022) 105617. https://doi.org/10.1016/J.RINP.2022.105617.
[253] Z. wei Li et al., J. Alloy. Compd. 922 (2022) 166179. https://doi.org/10.1016/J.JALLCOM.2022.166179.